A novel pseudo-rigid body approach to the non-linear dynamics of soft micro-particles in dilute viscous flow

Jana Wedel [a],[*], Matjaž Hriberšek [b], Jure Ravnik [b], Paul Steinmann [a],[c]

[a] *Institute of Applied Mechanics, Universität Erlangen-Nürnberg, Germany*
[b] *Faculty of Mechanical Engineering, University of Maribor, Slovenia*
[c] *Glasgow Computational Engineering Center, University of Glasgow, UK*

ARTICLE INFO

ABSTRACT

We propose a novel, demonstrably effective, utmost versatile and computationally highly efficient pseudo-rigid body approach for tracking the barycenter and shape dynamics of soft, i.e. non-linearly deformable micro-particles dilutely suspended in viscous flow. Pseudo-rigid bodies are characterized by affine deformation and thus represent a first-order extension to the kinematics of rigid bodies. Soft particles in viscous flow are ubiquitous in nature and sciences, prominent examples, among others, are cells, vesicles or bacteria. Typically, soft particles deform severely due to the mechanical loads exerted by the fluid flow. Since the shape dynamics of a soft particle - a terminology that shall here also include its orientation dynamics - also affects its barycenter dynamics, the resulting particle trajectory as a consequence is markedly altered as compared to a rigid particle. Here, we consider soft micro-particles of initially spherical shape that affinely deform into an ellipsoidal shape. These kinematic conditions are commensurate with i) the affine deformation assumption inherent to a pseudo-rigid body and ii) the celebrated Jeffery-Roscoe model for the traction exerted on an ellipsoidal particle due to creeping flow conditions around the particle. Without loss of generality, we here focus on non-linear hyperelastic particles for the sake of demonstration. Our novel numerical approach proves to accurately capture the particular deformation pattern of soft particles in viscous flow, such as for example tank-treading, thereby being completely general regarding the flow conditions at the macro-scale and, as an option, the constitutive behavior of the particle. Moreover, our computational method is highly efficient and allows straightforward integration into established Lagrangian tracking algorithms as employed for the point-particle approach to track rigid particles in dilute viscous flow.

1. Introduction

While the suspension of rigid particles has been widely studied for decades and is considered consolidated, [1], (see several analytical ([2–6]), experimental ([7–11]), and computational ([12–20]) studies for spherical and non-spherical rigid particles), research in the field of soft deformable particles is less established, [21]. Nevertheless, there are relevant examples of suspensions, both of industrial and scientific interest, where the suspension consists of soft, non-linearly deformable micron- and submicron-sized particles (hereafter referred to as micro-particles) that have a non-spherical shape due to the deformability of the particles, [22]. These

* Corresponding author.
E-mail address: jana.wedel@fau.de (J. Wedel).

particles include microgels, filled polymers, [23], biological cells, [1,24], as well as liquid droplets, vesicles and liquid capsules, [25], with elastic or viscoelastic properties. To model or control systems which include these soft, deformable particles, the governing physics of the particle system must be well understood, [26]. However, detailed knowledge about the dynamics of various types of soft particles suspended in flows is often sparse, [27], so these particle suspensions remain one of the most pressing problems in science and engineering, leading to increasing interest from the scientific community, [1]. Unfortunately, the complexity, challenges and costs of both experimental techniques and analytical and computational approaches increase dramatically in the case of soft micro-particles, especially when a large number of particles need to be considered, which is often a limiting factor.

1.1. State of the art

The shape change of soft particles is predominantly caused by hydrodynamic-induced mechanical loads, with the shape dynamics being key to determining the effective rheology of the suspension, [25]. Observe that the effective rheology of colloidal suspensions with deformable inclusions can differ significantly from suspensions consisting of rigid particles, [2]. As noted by Sanagavarapu et al., [25], an effective non-Newtonian rheology may be observed even in dilute suspensions, where inter-particle interactions are negligible, due to the deformation of the particles by the hydrodynamics-induced mechanical loads.

Fröhlich and Sack, [28], were arguably the first to study Hookean elastic, spherical particles suspended in a Newtonian fluid experiencing pure expansional motion. Later, Cerf, [29], considered an infinite dilute suspension of viscoelastic spheres in a viscous fluid subjected to small amplitude oscillatory motion. Oldroyd, [30], studied a dilute emulsion consisting of incompressible viscous droplets suspended in a viscous fluid, assuming a constant surface tension between the two phases. The analysis concluded that the deformation of the droplets and the surface tension lead to a suspension with effective visco-elastic behavior and an Oldroyd-type constitutive relationship. Another key step was Eshelby's approach for the confinement of an elastic inclusion in an elastic matrix, [31,32]. Goddard & Miller, [33], studied the time-dependent problem of slightly deformable visco-elastic spheres suspended in a Newtonian fluid under Stokes flow conditions. Taken together, the above authors ([28,29,33]) restricted their investigations of deformable elastic (and visco-elastic) particles to small deformations by assuming a simplifying linear constitutive relation for the elastic stress, [25].

Using the results of Jeffery, [6], for rigid ellipsoids and extending the work of Cerf, [29], Roscoe, [34], was the first to systematically investigate the suspension of initially spherical visco-elastic micro-particles (with either Neo-Hookean or Mooney-Rivlin elastic constitutive sub-models) in a viscous flow subjected to finite deformations. Roscoe found that initially spherical particles can obtain a stationary ellipsoidal shape with a fixed orientation in certain conditions (i.e. when suspended in shear flow) while the material within the ellipsoidal particle undergoes continuous deformation, i.e. the material points within the ellipsoid are in a tank-treading motion, [34]. Murata, [35], conducted a theoretical analysis using spherical harmonics of Hookean elastic particles suspended in an arbitrary Newtonian flow and observed that particles can deform to a steady-state shape. The author found that the suspended soft particle takes on an ellipsoidal shape if the particle is located at the stagnation point of a plane hyperbolic flow, [35]. In two dimensions Gao & Hu, [36], validated Roscoe's underlying assumption of affine deformation numerically. They studied two-dimensional, initially circular and elastic particles suspended in viscous shear flow and observed that after an initial transient deformation, a steady state with elliptical particle shape and tank-treading motion is reached. Later, Gao et al., [37], extended the validation of Roscoe's assumptions to the three-dimensional case. In this context, they studied the shape dynamics of elastic, initially spherical Neo-Hookean ellipsoids suspended in Stokes flow of a viscous fluid. The authors employed a polarization technique to obtain a theoretical framework for describing the shape and orientation dynamics of the elastic particles. The authors observed the predicted tank-treading motion in the ellipsoidal equilibrium shape.

Finally, Gao et al., [38], extended the analysis to elastic particles with an initially prolate spheroidal shape that move in a planar shear flow. Based on Eshelby's approach ([31,32]), they obtained a set of coupled nonlinear ordinary differential equations for the shape (half axes and orientation) and stress components. They employed fourth-order shape tensors to relate the stress rate to the strain rate of the particle. An important observation of this study was that, in addition to the tumbling regime in the quasi-rigid particle limit, a trembling regime was identified for the first time. In a later work, see [39], the authors investigated initially elliptical particles (2D) with arbitrary initial orientation suspended in an extensional flow using the polarization technique. Here, the authors report that the steady-state shape obtained in an extensional flow deviates from the steady-state shape of a particle suspended in a shear flow. The authors observed that the particle deforms in the former to an elliptical steady-state shape, with the long axis of the particle aligned with the extensional direction of the flow.

The works of Gao et al., [36–39], rely on the upper convective time derivative of the Neo-Hooke constitutive relation to determine the relationship between the stress rate and the strain rate. Sanagavarapu et al., [25], emphasize however that in more general constitutive relations such as, e.g., the Mooney-Rivlin constitutive model, despite the strain rate also the total strain appears in the expression for stress rate and thus cannot be related to strain rate alone. Therefore, the authors propose to take the conventional approach in incompressible hyperelasticity and directly relate the total stress to the total strain, [25]. They also note that such an approach to soft particle shape dynamics offers further insight into the underlying physics, since, for example, the orientation of soft particles is also influenced by hydrodynamics-induced strain and rotation.

Observe that all of the above authors studied initially stress-free spherical or ellipsoidal particles under restrictive assumptions regarding the flow conditions on the macro-scale and/or the constitutive behavior of the soft particles in order to allow either for analytical and/or computational solutions, the latter typically at significant computational cost.

In addition to the fluid-structure model such as presented above or immersed boundary techniques (see p.e. [40]) for soft deformable solids suspended in flows, another approach to track soft deformable particles in flows is the fluid-fluid approach, which

models the interactions between two fluids that are typically separated by an interface, [21]. In this context, Rosti and Brandt, [41], studied hyperelastic deformable particles of initially spherical shape suspended in a Couette flow at low Reynolds number. The authors solve the fluid-structure interaction problem with a one-continuum formulation, [41]. We would like to draw attention to the recent review article by Silva et al., [21], which provides an overview of the models available to simulate the transport of suspended, deformable, fluid-filled bodies and their interaction in a Newtonian fluid. The authors present different models for the treatment of fluid-structure and fluid-fluid interface, while focusing in the hydrodynamic part on the lattice Boltzmann method, [21]. As Silva et al., [21], state, fluid-structure models are computationally more demanding than fluid-fluid models, as the interface does not have to be explicitly tracked in the latter. However, the authors point out that the disadvantage of fluid-fluid models is that they do not provide sufficient control over the mechanical properties of the interfaces, which are often required in biological applications. Another critical point related to fluid-fluid models is that, to date, spurious currents occur at the interface, which, as Silva et al., [21], noted, arise as a result of the lack of sufficient isotropy of the underlying grid. Although the fluid-structure models are computationally more demanding, they provide better control over the interface (i.e. its mechanical properties) and consequently over the shape of the deformed particle. In addition, fluid-structure models do not introduce undesirable currents and offer considerable freedom in the shape space. The computational effort increases with the explicit consideration of the shape dynamics and consequently with the number of soft particles investigated and the number of degrees of freedom employed per particle, which depend on the discretization, i.e. the particle mesh.

### 1.2. General applications involving soft deformable particles suspended in flows

In this section we give a more detailed overview of applications for soft, deformable particles suspended in flows. Soft particles are becoming increasingly important in areas such as pharmaceutics and medicine, as they can be used as flexible microparticulate drug carriers, [42]. One example is liposomes, which are among the most widely used and well-studied therapeutic agents, [43]. Liposomes are increasingly popular in areas such as cancer diagnosis and treatment, [44]. Research in this area includes, among others [45–51], which mainly focused on the dynamics of vesicles and capsules. In recent years, self-propelling microorganisms have gained importance in fields such as biology and medicine, [1]. Zhao et al., [52] modeled a jellyfish in 2D assuming a Neo-Hooke elastic model. In addition, Nasouri et al., [53] modeled a two-sphere swimmer consisting of a rigid and a neo-Hookean sphere connected by a rod with periodically varying rod length. The authors report that the deformability of one part of the object, i.e. the neo-Hookean sphere, allows the object to move in the suspension (Newtonian fluid). Another important application for soft, deformable particles is the measurement of mechanical properties. Recently, Gerum et al., [54], developed an effective microfluidic shear flow deformation cytometry method in which the shear flow-induced deformation of cells into an ellipsoidal shape with observed tank-treading motion can be used to determine the viscoelastic properties of cells, including the elastic and viscous modulus. Another important application of soft deformable particles is in the field of particle separation. As Villone and Maffettone, [1], noted, the separation of small suspended particles is an important step in a variety of biological and chemical applications. In this context, Villone et al., [55] investigated the separation of elastic neo-Hookean beads based on their deformation while suspended in a Newtonian fluid in a T-shaped bifurcation. The authors observed that when the flow is evenly split between the outflow branches, stiffer particles migrate straight, while particles with a higher Capillary number, i.e. softer particles, tend to migrate to the side branch. The novel model presented in this work is intended to shed light on soft, deformable solid particles suspended in liquids, as they occur in applications involving suspensions of microgels, filled polymers and biological fluids. The present model is the ideal launching pad to model more complex behaviors, such as non-spherical initial particle shapes, surface tension, etc, in future works, as it is easily extendable to capture more physics

1.3. Pseudo-rigid body approach for soft deformable micro-particles in dilute flows

In this work, based on the heretofore mostly overlooked pseudo-rigid body theory, [56], that perfectly matches the kinematic conditions of soft ellipsoidal micro-particles in viscous flows, we propose a novel, utmost versatile, and highly efficient computational approach. It is straightforward to extend the model to non-spherical initial shapes, different material models and the consideration of surface tension. In addition, the model is not restricted to specific flow conditions, (usually in the literature models are derived for simple shear flow or extensional flow [25,36–39]) and is therefore more general and can readily be employed for particle tracking in any flow configuration as it can be coupled with any standard Lagrangian particle tracking. In general, pseudo-rigid bodies are characterized by affine deformation and thus represent a first-order extension to the kinematics of rigid bodies. To investigate the dynamics of large numbers of micro-particles in flow fields, the *point-particle approach* with Lagrangian particle tracking in combination with state-of-the-art computational solution of the Navier-Stokes equations is a general method of choice, [57]. However, without loss of generality and for demonstration purposes, analytical (or reported) flow fields are used in this work. The point-particle approach is advantageous due to its comparatively low computational cost, especially when a large number of particles are tracked, [58]. In the point-particle approach, the shape of a particle is not resolved, which is in contrast to the much more computationally intensive methods used in the soft particle literature presented above

The presented novel approach reproduces all of the challenging benchmark results from the pertinent literature, however without any of the typical restrictions and at minimal computational cost. Due to its low computational demand and straightforward integrability into the setting of established point-particle Lagrangian tracking algorithms for rigid particles, our approach is well suited to potentially capture a realistically large number, say $O(10^5 - 10^6)$, of soft, deformable micro-particles suspended in viscous fluids under general flow conditions.

Here, we consider tracking soft micro-particles in flows as a global-local, i.e. a two-scale problem. This is possible as we employ a one-way coupling approach, which resolves solely the impact of the fluid on the particle and not vice versa. Thus, we can independently address the update of the flow field from the particle problem. The *global problem at the macro-scale* consists of finding the fluid flow quantities at a given time step in a given macro-scale flow field. The local problem is twofold. The first *local problem at the micro-scale* consists of finding the deformed shape $\mathcal{B}_t$ (reducing to finding the orientation for rigid particles) for a given initial shape $\mathcal{B}_0$ and for given tractions t_t exerted by the flow on the particle, see Fig. 1. Given the new particle shape $\mathcal{B}_t$, the second *local problem at the micro-scale* is to obtain the particle's time-discrete barycenter trajectory within the fluid flow field. In this context, established force models f are employed that are based on the deformed particle shape $\mathcal{B}_t$. Note that on the micro-scale, the Reynolds numbers are typically well below one and thus the local flow around a micro-particle is safely assumed as viscous and accurately described by Stokes flow, [59].
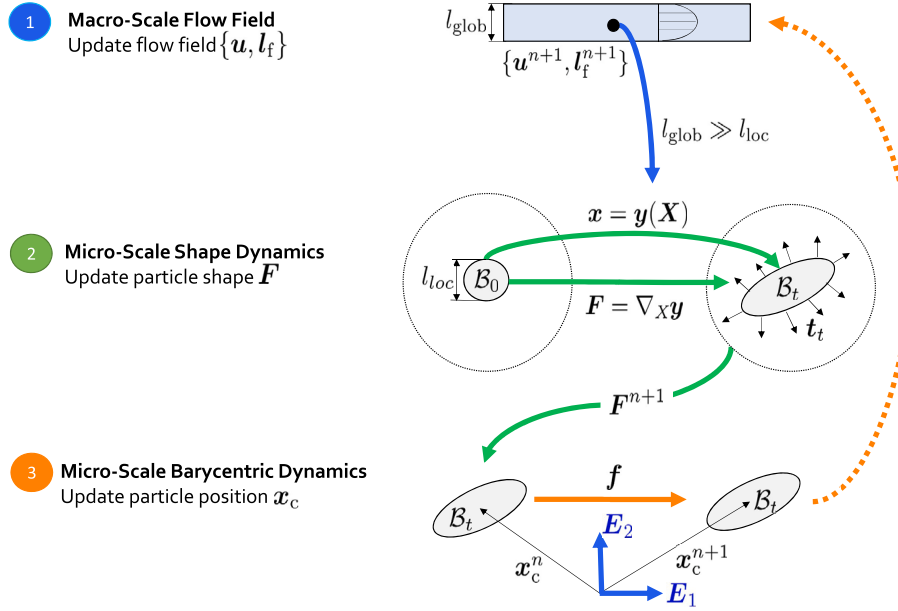
Fig. 1. Sketch of the novel pseudo-rigid body approach to the non-linear dynamics of soft micro-particles in viscous flow. Tracking soft micro-particles in flows is treated as a global-local, i.e. two-scale problem. In the macro-scale problem (global characteristic length l_{glob}) we solve for the flow field without accounting for the particle phase, i.e. one-way coupling approach. Then, the flow velocity u^{n+1} and the velocity gradient l_{f}^{n+1} at the current particle center x_{c} are obtained. On the micro-scale (local characteristic length l_{loc} with $l_{\text{loc}} \ll l_{\text{glob}}$) there are two separate problems. The first is denoted as shape dynamics and consists of finding the new particle shape F^{n+1}. Given the new particle shape, we can solve the second local problem, i.e. the barycentric dynamics, where we update the particle position x_{c} using established force models f. In the next time step, we first update the flow field (neglecting the particle influence on the fluid, since we consider one-way coupling). Next we can identify the new flow velocity u^{n+1} and the velocity gradient l_{f}^{n+1} at the particle position x_{c}^{n+1}, which are required inputs for the shape and barycentric dynamics.

1.4. Notation

In this work, we express tensors of various orders using bold italic font. First-order tensors (vectors) are denoted by bold italic lowercase letters such as a, while second-order tensors are denoted by bold italic uppercase letters such as A. Using Einstein's summation convention, we can write the coordinate representation in Cartesian coordinate systems with base vectors e_i', e_i ($i = 1, 2, 3$) as follows:

$$a = a_i' e_i' = a_i e_i \quad \text{and} \quad A = A_{ij}' e_i' \otimes e_j' = A_{ij} e_i \otimes e_j,$$

where a_i', a_i and A_{ij}', A_{ij} are the corresponding coefficients in the coordinate system e_i', e_i, respectively. The tensor coefficients a_i', a_i and A_{ij}', A_{ij} can be arranged in coefficient matrices, which we denote by underlined italic letters:

$$\underline{a}' = \begin{bmatrix} a_1' \\ a_2' \\ a_3' \end{bmatrix}, \quad \underline{a} = \begin{bmatrix} a_1 \\ a_2 \\ a_3 \end{bmatrix} \quad \text{and} \quad \underline{A}' = \begin{bmatrix} A_{11}' & A_{12}' & A_{13}' \\ A_{21}' & A_{22}' & A_{23}' \\ A_{31}' & A_{32}' & A_{33}' \end{bmatrix}, \quad \underline{A} = \begin{bmatrix} A_{11} & A_{12} & A_{13} \\ A_{21} & A_{22} & A_{23} \\ A_{31} & A_{32} & A_{33} \end{bmatrix}.$$

Note that the employed notation is based on our previous work, [18]. The rotation matrix $\underline{Q}$ transforming coefficients with respect to the base vectors e_i to coefficients with respect to the base vectors e_i' follows as

$$\underline{Q} = \begin{bmatrix} Q_{11} & Q_{12} & Q_{13} \\ Q_{21} & Q_{22} & Q_{23} \\ Q_{31} & Q_{32} & Q_{33} \end{bmatrix} \quad \text{with} \quad Q_{ij} = e'_i \cdot e_j \quad \text{and} \quad e'_i = Q_{ij} e_j . \tag{1}$$

The corresponding rotation tensor $\boldsymbol{Q} = e'_j \otimes e_j$ mapping e_j into $e'_j = \boldsymbol{Q} \cdot e_j$ has therefore coordinate representation $\boldsymbol{Q} = [e'_j \cdot e_i] e_i \otimes e_j = Q_{ji} e_i \otimes e_j$, i.e. the coefficient matrix of $\boldsymbol{Q}$ is the matrix transpose $\underline{Q}^T$. Taken together, coefficient matrices of vectors and second order tensors transform as

$$\underline{a}' = \underline{Q}\,\underline{a} \quad \text{and} \quad \underline{A}' = \underline{Q}\,\underline{A}\,\underline{Q}^T . \tag{2}$$

1.5. Outline

To set the stage, Sect. 2 recalls the non-linear kinematics, Lagrangian and resulting dynamics of a pseudo-rigid body. Next, Sect. 3 first reviews the Jeffery and Roscoe traction exerted on rigid and soft ellipsoidal micro-particles in viscous flow and then derives the resultant force and force dyad acting on a pseudo-rigid body. Subsequently, Sect. 4 proposes an implicit-explicit time-stepping algorithm for the determination of the discrete phase space trajectory following the barycenter and shape dynamics of a pseudo-rigid body. Finally, in Sect. 5, our approach is comprehensively validated by application to demonstrative benchmarks for the dynamics of soft micro-particles in, for example, rotational, simple shear and pipe flow. To close, Sect. 6 summarizes the paper and presents the main conclusions.

2. Pseudo-rigid body dynamics

This section first briefly reiterates the dynamics of pseudo-rigid bodies in the sense of Cohen and Muncaster [56] that we use as a modeling framework for soft deformable micro-particles suspended in Stokes flow.
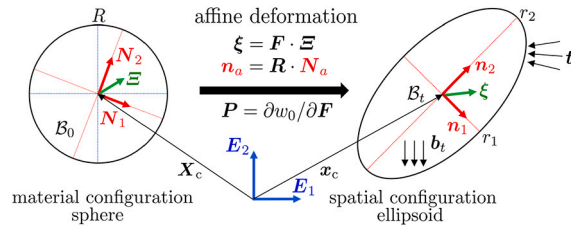

Fig. 2. Example of a pseudo-rigid body: Affine deformation of a sphere into an ellipsoid. Notation: Radius of a sphere $R > 0$ deforming into the half axes of an ellipsoid $r_1 = \lambda_1 R, r_2 = \lambda_2 R, r_3 = \lambda_3 R > 0$; Relative material and spatial positions $\boldsymbol{\Xi}$ and $\boldsymbol{\xi}$ connecting the barycenter with the material and spatial positions $\boldsymbol{X}$ in the material configuration $\mathcal{B}_0$ and $\boldsymbol{x}$ in the spatial configuration $\mathcal{B}_t$, respectively, of a pseudo-rigid body; Lagrangian principal directions $\boldsymbol{N}_a$ in the material configuration $\mathcal{B}_0$ and Eulerian principal directions $\boldsymbol{n}_a$ in the spatial configuration $\mathcal{B}_t$ with $a = 1, 2, 3$ (note that $\boldsymbol{N}_a$ and $\boldsymbol{n}_a$ are *not* body-fixed, i.e. they rather float through the body depending on the deformation); Fixed inertial frame of reference $\boldsymbol{E}_A$ with $A = 1, 2, 3$ (iFoR); Spatial bulk and surface force density $\boldsymbol{b}_t$ and $\boldsymbol{t}_t$, respectively.

2.1. Kinematics of a pseudo-rigid body

Let $\mathcal{B}_0$ and $\mathcal{B}_t$ denote the material and spatial configurations of a solid continuum body $B = \{P\}$ consisting of physical points P. Then the material positions $\boldsymbol{X} \in \mathcal{B}_0$ of the physical points P are taken to their spatial positions $\boldsymbol{x} \in \mathcal{B}_t$ by the deformation map $\boldsymbol{x} = \boldsymbol{y}(t, \boldsymbol{X})$, a nonlinear vector-valued function of time and space. The mass density (of the solid material) per unit volume in $\mathcal{B}_0$ is denoted[1] as ρ_0^s, a scalar-valued function of $\boldsymbol{X}$; its counterpart in the spatial configuration $\mathcal{B}_t$ is denoted as ρ_t^s.

The material positions $\boldsymbol{X}$ of a pseudo-rigid body, see the example in Fig. 2, are parameterized by the material position $\boldsymbol{X}_c$ of its barycenter and the relative material position $\boldsymbol{\Xi}$ as

$$\boldsymbol{X} = \boldsymbol{X}_c + \boldsymbol{\Xi} \quad \text{with} \quad \boldsymbol{\Xi} := \boldsymbol{X} - \boldsymbol{X}_c \quad \text{and the barycenter condition} \quad \int_{\mathcal{B}_0} \rho_0^s \boldsymbol{\Xi} \, dV \equiv \boldsymbol{0}, \tag{3}$$

with the material volume element dV. Then the deformation map $\boldsymbol{y}(t, \boldsymbol{X})$ of a pseudo-rigid body is composed of the motion $\boldsymbol{x}_c = \boldsymbol{y}_c(t)$ of its barycenter and its shape change $\boldsymbol{\xi}(t, \boldsymbol{\Xi})$, a superposed, affine deformation given by the (spatially uniform) deformation gradient $\boldsymbol{F}(t)$, a two-point tensor, as

$$\boldsymbol{x} = \boldsymbol{y}(t, \boldsymbol{X}) = \boldsymbol{y}_c(t) + \boldsymbol{\xi}(t, \boldsymbol{\Xi}) \quad \text{with} \quad \boldsymbol{X}_c = \boldsymbol{y}_c(t = 0) \quad \text{and} \quad \boldsymbol{\xi} := \boldsymbol{F}(t) \cdot \boldsymbol{\Xi} \quad \text{with} \quad \boldsymbol{1} = \boldsymbol{F}(t = 0). \tag{4}$$

Here $\boldsymbol{1}$ denotes the two-point unit tensor (with coefficients δ_{iJ}, i.e. the Kronecker-delta). The material volume element dV is mapped by the Jacobian $J := \det \boldsymbol{F} > 0$ of the deformation gradient into the spatial volume element $dv = J \, dV$, a relation that, due to J being

---

[1] In order to simplify the notation as much as possible, we only use super- or subscripts $(\bullet)^s$, $(\bullet)_s$ and $(\bullet)^f$, $(\bullet)_f$ indicating whether a property (superscript) or kinematic quantity (subscript) $(\bullet)$ refers to the solid or the fluid embedding it, if there is otherwise a risk of confusion.

spatially uniform, also holds for the total volumes $\mathrm{vol}(\mathcal{B}_t)$ and $\mathrm{vol}(\mathcal{B}_0)$ occupied by the pseudo-rigid body in its spatial and material configuration, thus $\mathrm{vol}(\mathcal{B}_t) = J\,\mathrm{vol}(\mathcal{B}_0)$. The velocities of the physical points P of the pseudo-rigid body are defined as the material time derivative of the deformation map and result in the decomposed representation

$$\boldsymbol{v} := \boldsymbol{v}_c(t) + \boldsymbol{v}(t, \boldsymbol{\Xi}) \quad \text{with} \quad \boldsymbol{v}_c := \dot{\boldsymbol{y}}_c(t) \quad \text{and} \quad \boldsymbol{v} := \dot{\boldsymbol{\xi}}(t, \boldsymbol{\Xi}) = \dot{\boldsymbol{F}}(t) \cdot \boldsymbol{\Xi} =: \boldsymbol{A}(t) \cdot \boldsymbol{\Xi}, \tag{5}$$

whereby the material velocity gradient $\dot{\boldsymbol{F}}$ is abbreviated as $\boldsymbol{A} := \dot{\boldsymbol{F}}$.

Remark *(Ellipsoidal Spatial Shape Resulting from Spherical Material Shape of a Pseudo-Rigid Body)*. Due to the condition $J > 0$ the deformation gradient $\boldsymbol{F}$ allows unique (right and left) polar decompositions into a properly orthogonal tensor $\boldsymbol{R}$, the continuum rotation tensor with $\boldsymbol{R}^t \equiv \boldsymbol{R}^{-1}$ and $\det \boldsymbol{R} = 1$, and positive definite symmetric tensors, either $\boldsymbol{U}$, the right stretch tensor with $\boldsymbol{U}^t \equiv \boldsymbol{U}$ and $\det \boldsymbol{U} > 0$, or $\boldsymbol{V}$, the left stretch tensor with $\boldsymbol{V}^t \equiv \boldsymbol{V}$ and $\det \boldsymbol{V} > 0$, as

$$\boldsymbol{F} = \boldsymbol{R} \cdot \boldsymbol{U} = \boldsymbol{V} \cdot \boldsymbol{R}. \tag{6}$$

In singular value (spectral) representation the continuum rotation and the stretch tensors expand as

$$\boldsymbol{R} = \sum_a \boldsymbol{n}_a \otimes \boldsymbol{N}_a, \quad \boldsymbol{U} = \sum_a \lambda_a \boldsymbol{N}_a \otimes \boldsymbol{N}_a \quad \text{and} \quad \boldsymbol{V} = \sum_a \lambda_a \boldsymbol{n}_a \otimes \boldsymbol{n}_a, \tag{7}$$

with $a = 1, 2, 3$ and $\boldsymbol{N}_a$ and $\boldsymbol{n}_a$ the orthonormal Lagrangian and Eulerian principal directions, see Fig. 2, and $\lambda_a > 0$ the corresponding principal stretches. The Lagrangian and Eulerian principal directions $\boldsymbol{N}_a$ and $\boldsymbol{n}_a$ are not body-fixed, rather they float through the body depending on the deformation gradient $\boldsymbol{F}$ that expands in singular value (spectral) representation as

$$\boldsymbol{F} = \sum_a \lambda_a \boldsymbol{n}_a \otimes \boldsymbol{N}_a. \tag{8}$$

Observe that $\boldsymbol{R}$ relates the Lagrangian principal directions $\boldsymbol{N}_a$ to the Eulerian principal directions $\boldsymbol{n}_a$ as

$$\boldsymbol{n}_a = \boldsymbol{R} \cdot \boldsymbol{N}_a. \tag{9}$$

When expressed in the fixed Cartesian frame $\boldsymbol{E}_A$ (the inertial frame of reference iFoR) with $A = 1, 2, 3$ the Eulerian principal directions $\boldsymbol{n}_a$, $a = 1, 2, 3$ follow via the rotation tensor $\boldsymbol{Q} := \boldsymbol{n}_b \otimes \boldsymbol{E}_B = [\boldsymbol{n}_b \cdot \boldsymbol{E}_A]\, \boldsymbol{E}_A \otimes \boldsymbol{E}_B$, $b \equiv B = 1, 2, 3$ as $\boldsymbol{n}_a = \boldsymbol{Q} \cdot \boldsymbol{E}_A$.

The polar decomposition of the deformation gradient $\boldsymbol{F}$ for a pseudo-rigid body with spherical shape in the material configuration $\mathcal{B}_0$ that is deformed by a uniform (affine) $\boldsymbol{F}$ to an ellipsoidal shape in the spatial configuration $\mathcal{B}_t$ is illustrated in Fig. 3.
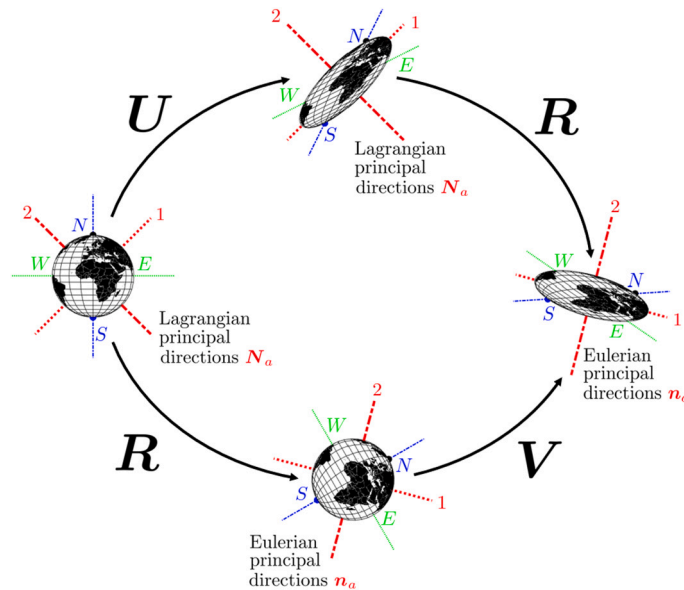
Fig. 3. Deformation of a pseudo-rigid body with spherical shape in the material configuration $\mathcal{B}_0$ (with $\mathrm{vol}(\mathcal{B}_0) = 3\pi R^3/4$ and $\boldsymbol{\Theta} = m R^2/5\,\boldsymbol{I}$) to an ellipsoidal shape in the spatial configuration $\mathcal{B}_t$. For clarity, the deformation is exemplified by a deformable planet, whereby the body-fixed, i.e. convecting axes connecting the north and south pole N and S and the west and the east pole W and E (parallel to the equator) together with the not body-fixed, i.e. deformation-dependent, free floating Lagrangian and Eulerian principal directions $\boldsymbol{N}_a$ and $\boldsymbol{n}_a$, $a = 1, 2, 3$ are highlighted. For a sphere with radius $R > 0$ in the material configuration $\mathcal{B}_0$ the half axes in the Lagrangian principal directions $\boldsymbol{N}_a$ are either first stretched by $\lambda_a > 0$, into their spatial counterparts $r_1 = \lambda_1 R, r_2 = \lambda_2 R, r_3 = \lambda_2 R > 0$ and then rotated by $\boldsymbol{R}$ into the Eulerian principal directions $\boldsymbol{n}_a$, or first rotated by $\boldsymbol{R}$ into the Eulerian principal directions $\boldsymbol{n}_a$ and then stretched by λ_a into r_a, to give the unique orientation of the deformed ellipsoid in the spatial configuration $\mathcal{B}_t$. Observe that the $N - S$ and $W - E$ axes convect with the deformation, i.e. are always attached to the same physical points of the planet, and thus do not remain orthogonal, whereas $\boldsymbol{N}_a$ and $\boldsymbol{n}_a$ are ortonormal triads.

2.2. Lagrangian of a pseudo-rigid body

The Lagrangian L of a pseudo-rigid body, a functional of the deformation map in terms of its barycenter and shape contributions, expands as

$$L := K(\boldsymbol{v}) - U(\boldsymbol{y}, \boldsymbol{F}) = K(\boldsymbol{v}_c, \boldsymbol{A}) - W(\boldsymbol{F}) - V(\boldsymbol{y}), \tag{10}$$

with K and U denoting the kinetic and the total potential energy, whereby U is the sum of the internal and the external potential energies W and V.

The kinetic energy K follows from an integral of its material density $k_0 = \rho_0^s |\boldsymbol{v}|^2/2$ over the bulk of the material configuration $\mathcal{B}_0$ of the pseudo-rigid body and, taking into account the barycenter condition[2], eventually results in

$$K = \frac{1}{2} \int_{\mathcal{B}_0} \rho_0^s |\boldsymbol{v}|^2 \mathrm{d}V = \frac{1}{2} m |\boldsymbol{v}_c|^2 + \frac{1}{2} \boldsymbol{\Theta} : [\boldsymbol{A}^t \cdot \boldsymbol{A}], \tag{11}$$

with the total mass m and the material Euler tensor $\boldsymbol{\Theta}$ of the pseudo-rigid body defined as

$$m := \int_{\mathcal{B}_0} \rho_0^s \mathrm{d}V \quad \text{and} \quad \boldsymbol{\Theta} := \int_{\mathcal{B}_0} \rho_0^s \, \boldsymbol{\Xi} \otimes \boldsymbol{\Xi} \, \mathrm{d}V. \tag{12}$$

Note that the shape contribution to the kinetic energy $\boldsymbol{\Theta} : [\boldsymbol{A}^t \cdot \boldsymbol{A}]/2$ is alternatively expressed in terms of the spatial Euler tensor $\boldsymbol{\theta} := \boldsymbol{F} \cdot \boldsymbol{\Theta} \cdot \boldsymbol{F}^t$ and the spatial velocity gradient $\boldsymbol{l}_s := \boldsymbol{A} \cdot \boldsymbol{F}^{-1}$ as

$$\frac{1}{2} \boldsymbol{\Theta} : [\boldsymbol{A}^t \cdot \boldsymbol{A}] \equiv \frac{1}{2} \boldsymbol{\theta} : [\boldsymbol{l}_s^t \cdot \boldsymbol{l}_s] \quad \text{with} \quad \boldsymbol{\theta} := \int_{\mathcal{B}_t} \rho_t^s \, \boldsymbol{\xi} \otimes \boldsymbol{\xi} \, \mathrm{d}v. \tag{13}$$

For hyperelastic pseudo-rigid bodies, the internal potential energy W expands as an integral of the stored energy density w_0, a function $w_0 = w_0(\boldsymbol{F})$ that will be specified below, over the bulk of the material configuration $\mathcal{B}_0$ of the pseudo-rigid body and, due to the spatial uniformity of $\boldsymbol{F}$, simplifies to

$$W = \int_{\mathcal{B}_0} w_0(\boldsymbol{F}) \mathrm{d}V = w_0(\boldsymbol{F}) \int_{\mathcal{B}_0} \mathrm{d}V =: w_0(\boldsymbol{F}) \operatorname{vol}(\mathcal{B}_0). \tag{14}$$

Finally the external potential energy V expands as an integral of its bulk and surface densities $v_0 = v_0(\boldsymbol{y})$ and $\hat{v}_0 = \hat{v}_0(\boldsymbol{y})$ over the bulk and surface of the material configuration $\mathcal{B}_0$ of the pseudo-rigid body

$$V = \int_{\mathcal{B}_0} v_0(\boldsymbol{y}) \mathrm{d}V + \int_{\partial \mathcal{B}_0} \hat{v}_0(\boldsymbol{y}) \mathrm{d}A. \tag{15}$$

The equations of motion for a pseudo-rigid body deriving from the Lagrangian L will be detailed in the sequel.

2.3. Barycenter dynamics

The Euler-Lagrange equation $\overline{\partial L/\partial \boldsymbol{v}_c} = \partial L/\partial \boldsymbol{y}_c$ governing the dynamics of the barycenter of a pseudo-rigid body results as

$$\dot{\boldsymbol{v}}_c \, m = \boldsymbol{f} \quad \text{with} \quad \boldsymbol{f} := \int_{\mathcal{B}_0} \boldsymbol{b}_0 \, \mathrm{d}V + \int_{\partial \mathcal{B}_0} \boldsymbol{t}_0 \, \mathrm{d}A \equiv \int_{\mathcal{B}_t} \boldsymbol{b}_t \, \mathrm{d}v + \int_{\partial \mathcal{B}_t} \boldsymbol{t}_t \, \mathrm{d}a. \tag{16}$$

Here, the force $\boldsymbol{f}$ is the resultant of the conservative bulk and surface force densities, the latter commonly denoted as the traction, that are defined as

$$\boldsymbol{b}_0 := -\frac{\partial v_0}{\partial \boldsymbol{y}} \quad \text{with} \quad \boldsymbol{b}_0 \, \mathrm{d}V \, (=: \boldsymbol{a} \, \rho_0^s \, \mathrm{d}V) \equiv \boldsymbol{b}_t \, \mathrm{d}v \, (=: \boldsymbol{a} \, \rho_t^s \, \mathrm{d}v) \quad \text{and} \quad \boldsymbol{t}_0 := -\frac{\partial \hat{v}_0}{\partial \boldsymbol{y}} \quad \text{with} \quad \boldsymbol{t}_0 \, \mathrm{d}A \equiv \boldsymbol{t}_t \, \mathrm{d}a, \tag{17}$$

where $\partial \boldsymbol{y}/\partial \boldsymbol{y}_c = \boldsymbol{i}$ with $\boldsymbol{i}$ the spatial unit tensor (with coefficients δ_{ij}, i.e. the Kronecker-delta) has tacitly been used. For spatially uniform mass-specific bulk force density $\boldsymbol{a}$ (with dimension of an acceleration) the corresponding contribution to $\boldsymbol{f}$ simplifies to $\boldsymbol{a} \, m$. The traction $\boldsymbol{t}_0$ is furthermore decomposed into its surface average $\bar{\boldsymbol{t}}_0$, a constant vector, and a fluctuation $\tilde{\boldsymbol{t}}_0$ as

---

[2] The squared velocity expands into

$$|\boldsymbol{v}|^2 = |\boldsymbol{v}_c + \boldsymbol{v}|^2 = |\boldsymbol{v}_c|^2 + |\boldsymbol{v}|^2 + 2\boldsymbol{v}_c \cdot \boldsymbol{v} = |\boldsymbol{v}_c|^2 + [\boldsymbol{\Xi} \otimes \boldsymbol{\Xi}] : [\boldsymbol{A}^t \cdot \boldsymbol{A}] + 2\boldsymbol{v}_c \cdot \boldsymbol{A} \cdot \boldsymbol{\Xi}.$$

When multiplied by ρ_0^s, and upon integration, the first and the second term on the right result in $m |\boldsymbol{v}_c|^2$ and $\boldsymbol{\Theta} : [\boldsymbol{A}^t \cdot \boldsymbol{A}]$, whereas the last term vanishes due to the barycenter condition.

$$t_0 = \bar{t}_0 + \tilde{t}_0 \quad \text{with} \quad \bar{t}_0 := \frac{1}{\text{sur}(\partial B_0)} \int\limits_{\partial B_0} t_0 \, dA \quad \text{and} \quad \boldsymbol{0} \equiv \int\limits_{\partial B_0} \tilde{t}_0 \, dA, \tag{18}$$

with $\text{sur}(\partial B_0)$ denoting the surface area of the pseudo-rigid body in its material configuration. The corresponding contribution to $\boldsymbol{f}$ thus simplifies to $\bar{t}_0 \, \text{sur}(\partial B_0)$. Analogous relations and consequences hold for the traction t_t with $\bar{t}_t \, \text{sur}(\partial B_t) \equiv \bar{t}_0 \, \text{sur}(\partial B_0)$.

The above equation of motion for the barycenter of a pseudo-rigid body is also valid for non-conservative bulk and surface force densities, the only difference being that no external potential energy densities exist.

2.4. Shape dynamics

The Euler-Lagrange equation $\overline{\partial L / \partial \dot{A}} = \partial L / \partial F$ governing the dynamics of the shape of a pseudo-rigid body results in two-point description as

$$\dot{A} \cdot \boldsymbol{\Theta} + P \, \text{vol}(B_0) = M \quad \text{with} \quad M := \int\limits_{B_0} b_0 \otimes \Xi \, dV + \int\limits_{\partial B_0} t_0 \otimes \Xi \, dA. \tag{19}$$

Here, the force dyad M, a two-point tensor, is the resultant of the dyadic moment of the bulk and surface force densities with Ξ. Finally, the Piola stress P, a two-point tensor, follows from the stored energy density w_0 as

$$P := \frac{\partial w_0}{\partial F}. \tag{20}$$

By a right-sided push-forward with F^t the above equation of motion for the shape of a pseudo-rigid body reads equivalently in spatial description as

$$[\dot{l}_s + l_s \cdot l_s] \cdot \boldsymbol{\theta} + \boldsymbol{\sigma} \, \text{vol}(B_t) = m \quad \text{with} \quad m := \int\limits_{B_t} b_t \otimes \boldsymbol{\xi} \, dv + \int\limits_{\partial B_t} t_t \otimes \boldsymbol{\xi} \, da, \tag{21}$$

where $\boldsymbol{\sigma}$ denotes the Cauchy stress, a spatial tensor, that relates to the Kirchhoff stress $\boldsymbol{\tau} := J \boldsymbol{\sigma} = P \cdot F^t$ via the Jacobian J, and $m := M \cdot F^t$ is the spatial force dyad.

Observe that for spatially uniform mass-specific bulk force density $\boldsymbol{a}$ the corresponding contribution to the force dyad M (and equivalently to $m = M \cdot F^t$) vanishes identically due to the barycenter condition. Furthermore, for the case of spherically symmetric distribution of mass density ρ_0^s the center of volume and the center of surface of an initially spherical pseudo-rigid body coincide with its barycenter (its center of mass)[3], i.e.

---

[3] Consider a unit sphere S(2) with barycenter coordinates $\bar{\Xi} \in \bar{B}_0$, radial coordinate $\bar{\Xi}(\bar{\Xi}) := |\bar{\Xi}| \leq 1$, unit director $\bar{N} := \bar{\Xi}/\bar{\Xi}$ and spherically symmetric mass density distribution $\bar{\rho}_0^s = \bar{\rho}_0^s(\bar{\Xi})$. Then the barycenter follows as

$$\int\limits_{\bar{B}_0} \bar{\rho}_0^s(\bar{\Xi}) \, \bar{\Xi} \, d\bar{V} = \int\limits_{\bar{B}_0} \bar{\rho}_0^s(\bar{\Xi}) \, \bar{\Xi} \, \bar{N} \, d\bar{V} = \int\limits_0^1 \bar{\rho}_0^s(\bar{\Xi}) \, \bar{\Xi} \, d\bar{\Xi} \int\limits_{\bar{\Omega}} \bar{N} \, d\bar{\Omega} = \boldsymbol{0} \quad \text{with} \quad \int\limits_{\bar{\Omega}} \bar{N} \, d\bar{\Omega} = \boldsymbol{0}.$$

Here $\bar{\Omega}$ and $d\bar{\Omega}$ denote the solid angle and its differential. By setting $\bar{\rho}_0^s = 1$ the center of volume also follows as $\bar{\Xi} = \boldsymbol{0}$. The surface of the unit sphere is given by the level set $\bar{\Xi} = 1$ with outwards pointing unit normal $\bar{N}$, thus the center of surface follows from the surface theorem as

$$\int\limits_{\partial \bar{B}_0} \bar{\Xi} \, d\bar{A} = \int\limits_{\partial \bar{B}_0} \bar{\Xi} \, \bar{N} \, d\bar{A} = \int\limits_{\partial \bar{B}_0} \bar{N} \, d\bar{A} = \int\limits_{\partial \bar{B}_0} d\bar{A} = \boldsymbol{0}.$$

The above shows that for a unit sphere with spherically symmetric mass density distribution the barycenter, the center of volume, and the center of surface coincide.

Consider next an affine mapping $\boldsymbol{\xi} = \bar{F} \cdot \bar{\Xi} \in B_t$ with constant $\bar{F}$, $\bar{J} := \det \bar{F} > 0$, from the unit sphere to an ellipsoid (or for $\bar{F} = R \, \boldsymbol{1}$ to a non-unit sphere of radius R). With $\bar{f} := \bar{F}^{-1}$ the radial coordinate parameterized in $\boldsymbol{\xi}$ reads as $\xi_{\bar{c}}(\boldsymbol{\xi}; \bar{c}) := |\boldsymbol{\xi} \cdot \bar{c} \cdot \boldsymbol{\xi}| \leq 1$ in the metric $\bar{c} := \bar{f}^t \cdot \bar{f}$. For the barycenter, it thus follows that

$$\int\limits_{B_t} \rho_t^s(\xi_{\bar{c}}) \, \boldsymbol{\xi} \, dv = \int\limits_{\bar{B}_0} [\bar{\rho}_0^s(\bar{\Xi})/\bar{J}] \, [\bar{F} \cdot \bar{\Xi}] \, [\bar{J} \, d\bar{V}] = \bar{F} \cdot \int\limits_{\bar{B}_0} \bar{\rho}_0^s(\bar{\Xi}) \, \bar{\Xi} \, d\bar{V} = \boldsymbol{0}.$$

The surface of the ellipsoid is given by the level set $\xi_{\bar{c}}(\boldsymbol{\xi}) = 1$ with outwards pointing unit normal $\boldsymbol{n} := p(\bar{N}; \bar{f}) \, \bar{f}^t \cdot \bar{N}$ where $\bar{f} \cdot \boldsymbol{\xi} = \bar{\Xi} \equiv \bar{N}$ holds at the surface (thus $\bar{c} \cdot \boldsymbol{\xi} = \bar{f}^t \cdot \bar{N}$) and with the function $p(\bar{N}; \bar{f}) = |\bar{f}^t \cdot \bar{N}|^{-1}$ that is periodic and positive over the surface. Then for computing the area center, $\boldsymbol{\xi}$ is decomposed into normal and tangential parts, i.e. $\boldsymbol{\xi} = \boldsymbol{\xi}_n + \boldsymbol{\xi}_t$, with $\boldsymbol{\xi}_n := \xi_n \boldsymbol{n}$ and $\xi_n := \boldsymbol{\xi} \cdot \boldsymbol{n}$. From $\boldsymbol{\xi} \cdot \bar{c} \cdot \boldsymbol{\xi} = [\boldsymbol{\xi} \cdot \boldsymbol{n}]/p(\bar{N}; \bar{f}) = 1$ it holds that $\xi_n = p(\bar{N}; \bar{f})$. Furthermore, the surface gradient $\hat{\nabla}_t(\bullet) := \nabla_t(\bullet) \cdot [\boldsymbol{i} - \boldsymbol{n} \otimes \boldsymbol{n}]$ of the function $2 f(\boldsymbol{\xi}_t) = |\boldsymbol{\xi}_t|^2$ renders $\hat{\nabla}_t f = \boldsymbol{\xi}_t$. Then, with the Nanson formula and the surface divergence theorem evaluated on a smooth and closed ($\partial^2 B_t = \emptyset$) surface (for the details on continuum mechanics and differential geometry see Steinmann [60]) it follows that

$$\int\limits_{\partial B_t} \boldsymbol{\xi}_n \, da = \int\limits_{\partial B_t} \xi_n \boldsymbol{n} \, da = \bar{J} \, \bar{f}^t \cdot \int\limits_{\partial \bar{B}_0} p(\bar{N}; \bar{f}) \, d\bar{A} = \boldsymbol{0} \quad \text{and} \quad \int\limits_{\partial B_t} \boldsymbol{\xi}_t \, da = \int\limits_{\partial B_t} \hat{\nabla}_t f(\boldsymbol{\xi}_t) \, da = \int\limits_{\partial^2 B_t} f(\boldsymbol{\xi}_t) \, d\hat{l} = \boldsymbol{0}.$$

The above shows that also for an ellipsoid affinely mapped from a unit sphere with spherically symmetric mass density distribution the barycenter, the center of volume, and the center of surface coincide.

$$\frac{1}{m} \int_{B_0} \rho_0^s \, \Xi \, dV \stackrel{\text{symmetry}}{\equiv} \frac{1}{V} \int_{B_0} \Xi \, dV \equiv \frac{1}{A} \int_{\partial B_0} \Xi \, dA \equiv \mathbf{0} . \tag{22}$$

Due to the spatial uniformity of $\mathbf{F}$ and J, analogous relations hold for the integrals of ξ. As a consequence, the contribution of the traction $\mathbf{t}_0$ to the force dyad $\mathbf{M}$ (and equivalently of $\mathbf{t}_t$ to $\mathbf{m} = \mathbf{M} \cdot \mathbf{F}^t$) depends on its fluctuation $\tilde{\mathbf{t}}_0$ (and equivalently on $\tilde{\mathbf{t}}_t$) only, that is

$$\int_{\partial B_0} \mathbf{t}_0 \otimes \Xi \, dA \stackrel{\text{symmetry}}{\equiv} \int_{\partial B_0} \tilde{\mathbf{t}}_0 \otimes \Xi \, dA \quad \text{and} \quad \int_{\partial B_t} \mathbf{t}_t \otimes \xi \, da \stackrel{\text{symmetry}}{\equiv} \int_{\partial B_t} \tilde{\mathbf{t}}_t \otimes \xi \, da . \tag{23}$$

It is remarked that the transition to the common equations of motion of a rigid body is detailed in Appendix A.

Remark *(Quasi-Incompressible Neo-Hooke Hyperelasticity).* In the sequel we will assume without loss of generality a quasi-incompressible Neo-Hooke stored energy density $w_0 = w_0(\mathbf{F})$ as the most elementary non-linear hyperelastic model. Then the resulting Piola stress $\mathbf{P} = \partial w_0 / \partial \mathbf{F}$ expands as

$$\mathbf{P} = \mu^s \left[\mathbf{F} - \mathbf{F}^{-t} \right] + \lambda^s \ln J \, \mathbf{F}^{-t} , \tag{24}$$

with Lamé parameters λ^s and μ^s, the former controlling the compressibility and the latter denoting the shear modulus of the solid. The incompressible limit is obtained for $\lambda^s \to \infty$.

3. Resultant loading on a pseudo-rigid body

For an ellipsoidal body immersed in Stokes flow analytical results exist for the traction (fluctuation) $\tilde{\mathbf{t}}_t$ exerted on the surface of the ellipsoidal body. Jeffery [6] considered rigid ellipsoids, results that were extended by Roscoe [34] to deformable ellipsoids. Since the assumptions put forward in these works are compliant with those of an ellipsoidal pseudo-rigid body, the Jeffery-Roscoe traction (fluctuation) $\tilde{\mathbf{t}}_t$ constitutes the key ingredient to determine the resultant force dyad driving the shape dynamics of a pseudo-rigid body with spherical material shape. The force driving the barycenter dynamics results from the mass-specific bulk force density $\mathbf{a}$ (gravity and buoyancy) and the surface-average traction $\bar{\mathbf{t}}_t$ (drag), the resultant of the latter is here modeled by the Brenner approach [61,62]. This section briefly details the key steps and the final expressions for the resultant loading exerted by Stokes flow on a pseudo-rigid body.

3.1. Jeffery traction

By analytically solving Stokes flow equations for an incompressible Newtonian fluid (characterized by constant density ρ^f (due to incompressibility we need not distinguish between ρ_t^f and ρ_0^f), kinematic viscosity ν^f, and dynamic viscosity $\mu^f = \rho^f \nu^f$) in the vicinity of an immersed ellipsoidal rigid body (particle), Jeffery [6] deduced the traction (fluctuation) $\tilde{\mathbf{t}}_t$ exerted by the flow on the surface of the ellipsoidal rigid body in the format of

$$\tilde{\mathbf{t}}_t = [-\tilde{p}(\mathbf{d}_f)\, \mathbf{i} + \mu^f \, \tilde{\mathbf{s}}(\mathbf{d}_f, \mathbf{w})] \cdot \mathbf{n} . \tag{25}$$

Here $\tilde{p}$ and $\tilde{\mathbf{s}}$ are a spatially constant factor and a spatially constant (non-symmetric) and deviatoric second-order tensor, respectively, and $\mathbf{n}$ denotes the outwards pointing normal to the surface of the ellipsoid. The factor $\tilde{p} = \tilde{p}(\mathbf{d}_f)$ as well as the coefficients of $\tilde{\mathbf{s}} = \tilde{\mathbf{s}}(\mathbf{d}_f, \mathbf{w})$, with $\mathbf{d}_f$ and $\mathbf{w} := \mathbf{w}_f - \mathbf{w}_s$ the fluid rate of deformation tensor and the modified spin (vorticity) tensor (with $\mathbf{w}_s$ the spin tensor of the solid angular velocity vector), respectively, in the particle frame of reference (pFoR) that is oriented along the ellipsoidal half axes are assembled for convenience in Appendix B.

3.2. Roscoe traction

Roscoe [34] extended the analytical result of Jeffery [6] regarding the traction (fluctuation) $\tilde{\mathbf{t}}_t$ exerted by Stokes flow on the surface of an ellipsoidal rigid body to the case of an ellipsoidal deformable body. The final result reads

$$\tilde{\mathbf{t}}_t = \left[-\tilde{p}(\mathbf{d})\, \mathbf{i} + \mu^f \left[\tilde{\mathbf{s}}(\mathbf{d}, \mathbf{w}) + 2\, \mathbf{d}_s \right] \right] \cdot \mathbf{n} , \tag{26}$$

with the modified rate of deformation tensor $\mathbf{d} := \mathbf{d}_f - \mathbf{d}_s$ (recall also the already previously used definition of the modified spin (vorticity) tensor $\mathbf{w} := \mathbf{w}_f - \mathbf{w}_s$). Here and below $\mathbf{d}_s$ and $\mathbf{w}_s$ denote the rate of deformation tensor and the spin tensor for the deformable ellipsoid, i.e. $\mathbf{d}_s := \mathbf{l}_s^{\text{sym}}$ and $\mathbf{w}_s := \mathbf{l}_s^{\text{skw}}$ with $\mathbf{l}_s$ the spatial velocity gradient of the solid (recall the definition $\mathbf{l}_s := \mathbf{A} \cdot \mathbf{F}^{-1}$). For a deformable ellipsoid in Stokes flow the rate of deformation tensor $\mathbf{d}_s$ proves spatially homogeneous as confirmed by, e.g., Gao et al. [37,38], a kinematic condition compliant with the above assumptions of a pseudo-rigid body. Moreover, $\tilde{p} = \tilde{p}(\mathbf{d})$ and $\tilde{\mathbf{s}} = \tilde{\mathbf{s}}(\mathbf{d}, \mathbf{w})$ are as given by Jeffery [6] when evaluated in terms of the modified rate of deformation tensor $\mathbf{d} := \mathbf{d}_f - \mathbf{d}_s$ (and, as already used before in the Jefferey expressions, the modified spin (vorticity) tensor $\mathbf{w} := \mathbf{w}_f - \mathbf{w}_s$) and in the pFoR that is oriented along the half axes of the deformed ellipsoid (see Appendix B). Since the above Roscoe traction (fluctuation) is linear in the outwards pointing normal $\mathbf{n}$ to the surface of the ellipsoid, i.e. $\tilde{\mathbf{t}}_t = \tilde{\boldsymbol{\sigma}} \cdot \mathbf{n}$, it can finally be expressed in terms of a spatially uniform (constant) Cauchy-type stress $\tilde{\boldsymbol{\sigma}}$ expanding as

$$\tilde{\boldsymbol{\sigma}} = -\tilde{p}(\boldsymbol{d})\,\boldsymbol{i} + \mu^{\mathrm{f}}\left[\tilde{\mathrm{s}}(\boldsymbol{d},\boldsymbol{w}) + 2\,\boldsymbol{d}_{\mathrm{s}}\right]. \tag{27}$$

The key steps in the derivation of the Roscoe traction (fluctuation) $\tilde{\boldsymbol{t}}_t$, [34], exerted on a deformable ellipsoid in a viscous flow are summarized in Appendix C.

3.3. Resultant force

For spatially uniform mass-specific bulk force density $\boldsymbol{a}_{\mathrm{G}}$, an acceleration, the reduced gravity force $\boldsymbol{f}_{\mathrm{G}}$ (i.e. reduced by buoyancy) that is exerted on an ellipsoid in a fluid reads as

$$\boldsymbol{f}_{\mathrm{G}} = \boldsymbol{a}_{\mathrm{G}}\,m \quad \text{with} \quad \boldsymbol{a}_{\mathrm{G}} = \frac{\rho_t^{\mathrm{s}} - \rho^{\mathrm{f}}}{\rho_t^{\mathrm{s}}}\,\boldsymbol{g}, \tag{28}$$

with $\boldsymbol{g}$ the gravity acceleration assumed spatially uniform. Recall that the spatial mass density $\rho_t^{\mathrm{s}} = \rho_0^{\mathrm{s}}/J$ of the pseudo-rigid body is spatially uniform for the here assumed spatially uniform ρ_0^{s}, thus the total mass of the pseudo-rigid body reads as $m = \rho_t^{\mathrm{s}}\,\mathrm{vol}(\mathcal{B}_t)$. Moreover, due to its incompressibility, also the mass density of the fluid ρ^{f} is uniform (constant), thus the total fluid mass equivalent to the volume $\mathrm{vol}(\mathcal{B}_t)$ occupied by the pseudo-rigid body is simply $\rho^{\mathrm{f}}\,\mathrm{vol}(\mathcal{B}_t)$. In summary, the reduced gravity force reads as

$$\boldsymbol{f}_{\mathrm{G}} = [\rho_t^{\mathrm{s}} - \rho^{\mathrm{f}}]\,\boldsymbol{g}\,\mathrm{vol}(\mathcal{B}_t). \tag{29}$$

Moreover, we employ the drag expression for arbitrarily shaped bodies, i.e. particularly including ellipsoids, as proposed by Brenner, [61]. Thus, the drag force $\boldsymbol{f}_{\mathrm{D}}$ exerted on an ellipsoid in a viscous fluid is given as

$$\boldsymbol{f}_{\mathrm{D}} = \bar{\boldsymbol{t}}_t\,\mathrm{sur}(\partial\mathcal{B}_t) = \pi\,\mu^{\mathrm{f}}\,r_{\min}\,\boldsymbol{k}\cdot[\boldsymbol{u} - \boldsymbol{v}_{\mathrm{c}}], \tag{30}$$

where μ^{f} denotes the dynamic viscosity of the fluid, $r_{\min}$ the minor half axis of the ellipsoid, $\boldsymbol{k}$ its translational resistance tensor, and $\boldsymbol{u}$ and $\boldsymbol{v}_{\mathrm{c}}$ the velocity of the fluid at the barycenter of the ellipsoid and its barycentric velocity $\boldsymbol{v}_{\mathrm{c}}$. The coefficients of the translational resistance tensor in the pFoR are detailed in Appendix D.

Further contributions to $\boldsymbol{f}$ due to added mass and pressure gradient effects are negligible under the here considered conditions (locally small Stokes number, i.e. St $\ll$ 1). Taken together, the resultant force $\boldsymbol{f}$ exerted on an ellipsoid in a viscous fluid here combines as $\boldsymbol{f} = \boldsymbol{f}_{\mathrm{G}} + \boldsymbol{f}_{\mathrm{D}}$.

3.4. Resultant force dyad

Since the mass-specific bulk force density $\boldsymbol{a}$ is spatially uniform, the resultant force dyad $\boldsymbol{m}$ expands with $\tilde{\boldsymbol{t}}_t = \tilde{\boldsymbol{\sigma}}\cdot\boldsymbol{n}$ as[4]

$$\boldsymbol{m} = \int_{\partial\mathcal{B}_t} \tilde{\boldsymbol{t}}_t \otimes \boldsymbol{\xi}\,\mathrm{d}a = \int_{\partial\mathcal{B}_t} [\boldsymbol{\xi} \otimes \tilde{\boldsymbol{\sigma}}\cdot\mathrm{d}\boldsymbol{a}]^t = \int_{\mathcal{B}_t} [\mathrm{div}(\boldsymbol{\xi} \otimes \tilde{\boldsymbol{\sigma}})]^t\,\mathrm{d}v = \tilde{\boldsymbol{\sigma}}\,\mathrm{vol}(\mathcal{B}_t), \tag{31}$$

with $\mathrm{d}\boldsymbol{a} := \boldsymbol{n}\,\mathrm{d}a$ the vectorial area element on $\partial\mathcal{B}_t$. When introducing the Kirchhoff-type stress $\tilde{\boldsymbol{\tau}} := J\,\tilde{\boldsymbol{\sigma}}$ the resultant force dyad $\boldsymbol{m}$ expands as $\boldsymbol{m} = \tilde{\boldsymbol{\tau}}\,\mathrm{vol}(\mathcal{B}_0)$, furthermore with the Piola-type stress $\tilde{\boldsymbol{P}} := \tilde{\boldsymbol{\tau}}\cdot\boldsymbol{F}^{-t}$ the resultant force dyad $\boldsymbol{M} = \boldsymbol{m}\cdot\boldsymbol{F}^{-t}$ finally reads as

$$\boldsymbol{M} = \tilde{\boldsymbol{P}}\,\mathrm{vol}(\mathcal{B}_0). \tag{32}$$

Note that $\tilde{\boldsymbol{\sigma}}$, $\tilde{\boldsymbol{\tau}}$ and $\tilde{\boldsymbol{P}}$ derive from the (Jeffery and) Roscoe expressions for the traction (fluctuation) $\tilde{\boldsymbol{t}}_t$ exerted by Stokes flow on an ellipsoid.

4. Time stepping

In summary, the equations of motion describing the barycenter and shape dynamics of an ellipsoidal pseudo-rigid body (particle), spherical in $\mathcal{B}_0$, that is immersed in Stokes flow read in first-order ODE format as

$$\dot{\boldsymbol{x}}_{\mathrm{c}} = \boldsymbol{v}_{\mathrm{c}}, \quad \dot{\boldsymbol{v}}_{\mathrm{c}} = \boldsymbol{a}_{\mathrm{G}} + \boldsymbol{a}_{\mathrm{D}} \quad \text{and} \quad \dot{\boldsymbol{F}} = \boldsymbol{A}, \quad \dot{\boldsymbol{A}} = \mathrm{vol}(\mathcal{B}_0)\,[\tilde{\boldsymbol{P}} - \boldsymbol{P}]\cdot\boldsymbol{\Theta}^{-1}, \tag{33}$$

with the mass-specific reduced gravity and drag contributions to the resultant force

$$\boldsymbol{a}_{\mathrm{G}} := \boldsymbol{f}_{\mathrm{G}}/m =: \beta_t\,\boldsymbol{g} \quad \text{and} \quad \boldsymbol{a}_{\mathrm{D}} := \boldsymbol{f}_{\mathrm{D}}/m =: \frac{1}{\tau_{\mathrm{D}}}\,\boldsymbol{k}\cdot[\boldsymbol{u} - \boldsymbol{v}_{\mathrm{c}}]. \tag{34}$$

Here, β_t and τ_{D} denote the buoyancy-induced gravity reduction and the characteristic drag time, respectively, defined as

$$\beta_t := \frac{\rho_t^{\mathrm{s}} - \rho^{\mathrm{f}}}{\rho_t^{\mathrm{s}}} \quad \text{and} \quad \tau_{\mathrm{D}} := \frac{1}{\nu^{\mathrm{f}}}\,\frac{\rho_0^{\mathrm{s}}}{\rho^{\mathrm{f}}}\,\frac{4}{3}\,\frac{R^3}{r_{\min}}. \tag{35}$$

---

[4] Due to $\tilde{\boldsymbol{\sigma}} = $ constant the expression $\mathrm{div}(\boldsymbol{\xi} \otimes \tilde{\boldsymbol{\sigma}})$ results in $\tilde{\boldsymbol{\sigma}}^t$ as straightforwardly demonstrated in index notation $[\xi_i\,\tilde{\sigma}_{jk}]_{,k} = \delta_{ik}\,\tilde{\sigma}_{jk} = \tilde{\sigma}_{ji}$.

The time stepping algorithms (time integrators) for the integration of these evolution equations in discrete time steps $\Delta t := t^{n+1} - t^n$, with t^{n+1} and t^n discrete time points, over a finite time interval $T := \cup_{n=0}^{N-1}[t^{n+1} - t^n]$, i.e. over N discrete time steps Δt are detailed in the following. Therein we assume the barycenter position x_c^n and the barycenter velocity v_c^n together with the deformation gradient F^n and the material velocity gradient A^n of the pseudo-rigid body at the discrete time point t^n as well as the fluid velocity u^{n+1} together with the spatial fluid velocity gradient $l_f^{n+1} =: d_f^{n+1} + w_f^{n+1}$ at the discrete time point t^{n+1}, considered as the external loading for the time step Δt, be given for a given time step Δt.

4.1. Barycenter dynamics

Here we update the barycenter position x_c and the barycenter velocity v_c over Δt by the implicit Euler backwards time integrator

$$x_c^{n+1} = x_c^n + \Delta t\, v_c^{n+1} \quad \text{and} \quad v_c^{n+1} = v_c^n + \Delta t\,[a_G^{n+1} + a_D^{n+1}], \tag{36}$$

with the implicit update of the mass-specific reduced gravity and drag forces a_G^{n+1} and a_D^{n+1}

$$a_G^{n+1} := \beta_t^{n+1}\, g \quad \text{and} \quad a_D^{n+1} := \frac{1}{\tau_D}\, k^{n+1} \cdot [u^{n+1} - v_c^{n+1}]. \tag{37}$$

Thereby, the buoyancy-induced gravity reduction β_t^{n+1} and the translational resistance tensor k^{n+1} are updated as

$$\beta_t^{n+1} := \beta_t(F^{n+1}) \quad \text{and} \quad k^{n+1} := k(F^{n+1}), \tag{38}$$

where the dependence of β_t^{n+1} on F^{n+1} is via J^{n+1} and the dependence of k^{n+1} on F^{n+1} is via n_a^{n+1} and λ_a^{n+1} to update the pFoR with the rotation matrix $\underline{Q}^{n+1} := [Q_{aB}^{n+1}] = [n_a^{n+1} \cdot E_B]$, $a, B = 1, 2, 3$ and the ellipsoid's half axes $r_a^{n+1} = \lambda_a^{n+1}\, R$, $a = 1, 2, 3$, respectively.

Observe that due to the decoupled determination of F^{n+1} from the time stepping for the shape dynamics as detailed in the sequel, β_t^{n+1} and k^{n+1} are given quantities in the time stepping for the barycenter dynamics and do not require iterative updates within Δt, thus avoiding the need for cumbersome linearization with respect to F^{n+1}. The updates for x_c^{n+1} and v_c^{n+1} conceptually require the concurrent iterative solution of a coupled system in the two unknowns x_c^{n+1} and v_c^{n+1} with residua

$$r_x(x_c^{n+1}, v_c^{n+1}) := x_c^{n+1} - x_c^n - \Delta t\, v_c^{n+1} \doteq 0, \tag{39}$$

$$r_v(\text{---}, v_c^{n+1}) := v_c^{n+1} - v_c^n - \Delta t\left[a_G^{n+1} + \frac{1}{\tau_D}\, k^{n+1} \cdot [u^{n+1} - v_c^{n+1}]\right] \doteq 0. \tag{40}$$

However, the residual $r_x \doteq 0$ allows closed form solution $\Delta t\, v_c^{n+1} = x_c^{n+1} - x_c^n$ that can be inserted into $\Delta t\, r_v \doteq 0$ to result in a single linear residual in the unknown barycenter position x_c^{n+1} that reads

$$r(x_c^{n+1}) := x_c^{n+1} - x_c^n - \Delta t\, v_c^n - \Delta t^2\, a_G^{n+1} - \frac{\Delta t}{\tau_D}\, k^{n+1} \cdot [\Delta t\, u^{n+1} - x_c^{n+1} + x_c^n] \doteq 0. \tag{41}$$

Then, due to the linearity of the residual $r(x_c^{n+1})$ in the unknown x_c^{n+1} its solution follows in closed form as

$$x_c^{n+1} = -\Bbbk^{-1} \cdot r(0) \quad \text{with} \quad \Bbbk := i + \frac{\Delta t}{\tau_D}\, k^{n+1}. \tag{42}$$

The step-by-step algorithm for the implicit time integrator for the barycenter dynamics of a pseudo-rigid body with a spherical shape in the material configuration based on its barycenter position is given in Appendix E.

Remark (*Alternative Algorithm based on Barycenter Velocity*). Alternatively, due to its independence on x_c^{n+1} the solution of the residual $r_v(v_c^{n+1}) \doteq 0$ follows in closed form as

$$v_c^{n+1} = -\Bbbk^{-1} \cdot r_v(0) \tag{43}$$

Then, the residual $r_x \doteq 0$ allows closed form solution $x_c^{n+1} = x_c^n + \Delta t\, v_c^{n+1}$ rendering the same x_c^{n+1} as in the above.

4.2. Shape dynamics

Here we update the deformation gradient F over Δt by the implicit Euler backwards time integrator, whereas we update the material velocity gradient A over Δt by an implicit-explicit time integrator

$$F^{n+1} = F^n + \Delta t\, A^{n+1} \quad \text{and} \quad A^{n+1} = A^n + \Delta t\, \text{vol}(\mathcal{B}_0)\,[\tilde{P}^\star - P^{n+1}] \cdot \Theta^{-1}, \tag{44}$$

with the implicit update of the Piola stress P^{n+1} and the implicit-explicit update of the Piola-type stress $\tilde{P}^\star$, as denoted by a superscript star

$$P^{n+1} := P(F^{n+1}) \quad \text{and} \quad \tilde{P}^\star := J^{n+1}\, \tilde{\sigma}^\star \cdot [F^{n+1}]^{-t}. \tag{45}$$

Furthermore, the implicit-explicit update of the Cauchy-type stress $\tilde{\sigma}^\star$ is given as

$$\tilde{\sigma}^{\star} := \tilde{\sigma}(\boldsymbol{F}^n, \boldsymbol{A}^n; \boldsymbol{l}_{\mathrm{f}}^{n+1}). \tag{46}$$

The dependence of $\tilde{\sigma}^{\star}$ on $\boldsymbol{F}^n$ is via $\boldsymbol{n}_a^n$ and λ_a^n to update the pFoR with the rotation matrix $\underline{Q}^n := [Q_{aB}^n] = [\boldsymbol{n}_a^n \cdot \boldsymbol{E}_B]$, $a, B = 1, 2, 3$ and the ellipsoid's half axes $r_a^n = \lambda_a^n R$, $a = 1, 2, 3$. In addition, $\tilde{\sigma}^{\star}$ depends on $\boldsymbol{F}^n$ and $\boldsymbol{A}^n$ via the spatial solid velocity gradient $\boldsymbol{l}_{\mathrm{s}}^n = \boldsymbol{A}^n \cdot [\boldsymbol{F}^n]^{-1}$ with coefficients $l_{\mathrm{s}ab}^{\prime n}$ in the pFoR defined as $l_{\mathrm{s}ab}^{\prime n} := \boldsymbol{n}_a^n \cdot \boldsymbol{l}_{\mathrm{s}}^n \cdot \boldsymbol{n}_b^n$. Finally, $\tilde{\sigma}^{\star}$ is parameterized (as indicated in its argument list by the separation via a semi-colon) in the given $\boldsymbol{l}_{\mathrm{f}}^{n+1}$ with coefficients $l_{\mathrm{f}ab}^{\prime \star}$ in the pFoR defined as $l_{\mathrm{f}ab}^{\prime \star} := \boldsymbol{n}_a^n \cdot \boldsymbol{l}_{\mathrm{f}}^{n+1} \cdot \boldsymbol{n}_b^n$ and representing the external loading for Δt.

Observe that due to its implicit-explicit treatment, $\tilde{\sigma}^{\star}$ is a given quantity for Δt and does not require iterative updates within Δt, thus avoiding the need for its cumbersome linearization with respect to $\boldsymbol{F}^{n+1}$ and $\boldsymbol{A}^{n+1}$. Nevertheless, $\tilde{\boldsymbol{P}}^{\star}$ depends on $\boldsymbol{F}^{n+1}$, i.e. $\tilde{\boldsymbol{P}}^{\star} = \tilde{\boldsymbol{P}}^{\star}(\boldsymbol{F}^{n+1}; \tilde{\sigma}^{\star})$, thus the updates for $\boldsymbol{F}^{n+1}$ and $\boldsymbol{A}^{n+1}$ conceptually require the concurrent iterative solution of a coupled system in the two unknowns $\boldsymbol{F}^{n+1}$ and $\boldsymbol{A}^{n+1}$ with residua

$$\boldsymbol{R}_F(\boldsymbol{F}^{n+1}, \boldsymbol{A}^{n+1}) := \boldsymbol{F}^{n+1} - \boldsymbol{F}^n - \Delta t \, \boldsymbol{A}^{n+1} \doteq \boldsymbol{0}, \tag{47}$$

$$\boldsymbol{R}_A(\boldsymbol{F}^{n+1}, \boldsymbol{A}^{n+1}) := \boldsymbol{A}^{n+1} - \boldsymbol{A}^n - \Delta t \, \mathrm{vol}(\mathcal{B}_0) \left[\tilde{\boldsymbol{P}}^{\star}(\boldsymbol{F}^{n+1}; \tilde{\sigma}^{\star}) - \boldsymbol{P}(\boldsymbol{F}^{n+1}) \right] \cdot \boldsymbol{\Theta}^{-1} \doteq \boldsymbol{0}. \tag{48}$$

Since the residual $\boldsymbol{R}_F \doteq \boldsymbol{0}$ allows closed form solution $\Delta t \, \boldsymbol{A}^{n+1} = \boldsymbol{F}^{n+1} - \boldsymbol{F}^n$ that can be inserted into $\Delta t \, \boldsymbol{R}_A \doteq \boldsymbol{0}$, a single nonlinear residual in the unknown deformation gradient $\boldsymbol{F}^{n+1}$ results as

$$\boldsymbol{R}(\boldsymbol{F}^{n+1}) := \boldsymbol{F}^{n+1} - \boldsymbol{F}^n - \Delta t \, \boldsymbol{A}^n - \Delta t^2 \, \mathrm{vol}(\mathcal{B}_0) \left[\tilde{\boldsymbol{P}}^{\star}(\boldsymbol{F}^{n+1}; \tilde{\sigma}^{\star}) - \boldsymbol{P}(\boldsymbol{F}^{n+1}) \right] \cdot \boldsymbol{\Theta}^{-1} \doteq \boldsymbol{0}. \tag{49}$$

Then, the solution for $\boldsymbol{F}^{n+1}$ is obtained by a Newton iteration with iterative updates $\boldsymbol{F}^{n+1} \leftarrow \boldsymbol{F}^{n+1} - \mathbb{K}^{-1} : \boldsymbol{R}(\boldsymbol{F}^{n+1})$, whereby we determined the linearization $\mathbb{K} := \partial \boldsymbol{R} / \partial \boldsymbol{F}^{n+1}$, a two-point fourth-order tensor, in analytical format as

$$\mathbb{K} = \mathbb{I} - \Delta t^2 \, \mathrm{vol}(\mathcal{B}_0) \left[\tilde{\mathbb{A}}^{\star} - \mathbb{A} \right]^{\overset{21}{\cdot}} \boldsymbol{\Theta}^{-1} \quad \text{with} \quad \tilde{\mathbb{A}}^{\star} := \partial \tilde{\boldsymbol{P}}^{\star} / \partial \boldsymbol{F}^{n+1} \quad \text{and} \quad \mathbb{A} := \partial \boldsymbol{P}^{n+1} / \partial \boldsymbol{F}^{n+1}, \tag{50}$$

where $\mathbb{I}$ and $\overset{21}{\cdot}$ denote the two-point fourth-order unit tensor and single contraction of the second slot of $\tilde{\mathbb{A}}^{\star} - \mathbb{A}$ with the first slot of $\boldsymbol{\Theta}^{-1}$. The Newton iteration shows quadratic rate of convergence for the norm of the residual $|\boldsymbol{R}|$ until it falls under a given tolerance.

The step-by-step algorithm for the implicit-explicit time integrator for the shape dynamics of a pseudo-rigid body with spherical shape in the material configuration based on the deformation gradient is given in Appendix E. Note that a discussion on the efficiency of the algorithm is provided in Appendix F.

Remark (*Alternative Algorithm based on Material Velocity Gradient*). Alternatively, the residual $\boldsymbol{R}_F \doteq \boldsymbol{0}$ allows closed form solution $\boldsymbol{F}^{n+1} = \boldsymbol{F}^n + \Delta t \, \boldsymbol{A}^{n+1}$ that can be inserted into $\boldsymbol{R}_A \doteq \boldsymbol{0}$ to result in a single nonlinear residual in the unknown material velocity gradient $\boldsymbol{A}^{n+1}$ that reads

$$\boldsymbol{R}(\boldsymbol{A}^{n+1}) := \boldsymbol{A}^{n+1} - \boldsymbol{A}^n - \Delta t \, \mathrm{vol}(\mathcal{B}_0) \left[\tilde{\boldsymbol{P}}^{\star}(\boldsymbol{F}^n + \Delta t \, \boldsymbol{A}^{n+1}; \tilde{\sigma}^{\star}) - \boldsymbol{P}(\boldsymbol{F}^n + \Delta t \, \boldsymbol{A}^{n+1}) \right] \cdot \boldsymbol{\Theta}^{-1} \doteq \boldsymbol{0}. \tag{51}$$

Then, the solution for $\boldsymbol{A}^{n+1}$ is obtained by a Newton iteration with iterative updates $\boldsymbol{A}^{n+1} \leftarrow \boldsymbol{A}^{n+1} - \mathbb{K}^{-1} : \boldsymbol{R}(\boldsymbol{A}^{n+1})$.

5. Demonstrative examples

In the following, characteristic scales for the non-dimensionalization are chosen as the length scale d_{eq} (volume-equivalent particle diameter), the time scale $\dot{\gamma}^{-1}$ (inverse fluid shear rate), and the pressure/stress scale $\mu^{\mathrm{f}} \dot{\gamma}$. Then we employ the capillary number Ca as a dimensionless parameter representing the ratio of the viscous forces in the fluid to the elastic forces in the particle, [37] as

$$\mathrm{Ca} = \frac{\mu^{\mathrm{f}} \dot{\gamma}}{\mu^{\mathrm{s}}}. \tag{52}$$

Note that an increasing Ca is associated with a softer particle, [37]. The capillary number Ca defined in Eq. (52) differs from that for fluid vesicles as we employ μ^{s} with units N/m^2 instead of the membrane shear modulus in units N/m (as is common for vesicles), [36]. Note that μ^{f} has the units $N s/m^2$, while $\dot{\gamma}$ has the units s^{-1}. Here, the particle Reynolds number is defined using the shear rate $\dot{\gamma}$ as

$$\mathrm{Re} = \frac{\dot{\gamma} \, d_{\mathrm{eq}}^2}{\nu^{\mathrm{f}}} \tag{53}$$

and is required to be $\mathrm{Re} \ll 1$ for the Jeffery-Roscoe solution to hold. To describe the deformation of the particles, it is also useful to introduce the Taylor deformation parameter $\eth$, which is commonly used as a measure of the deformation of droplets and vesicles, [63]. The deformation parameter can be determined using the particle semi-axis ratio $\delta_1 = b/a$ (and $\delta_2 = c/a$) as follows [37]:

$$\eth = \frac{a - b}{a + b} = \frac{1 - \delta_1}{1 + \delta_1}. \tag{54}$$

As stated by Gao et al., [37], for Đ < 0.2, i.e. for stiff particles, the relation between Ca and Đ can be approximated as Đ = Ca. As the particles become softer (Ca ↗), a nonlinear relation can be observed, [37]. Furthermore, Gao et al., [37], observed, that for Ca → ∞ (for super small solid μ^s) one obtains Đ → 1 ($\delta_1 \to 0$), thus the particle behaves like a super soft particle.

5.1. Soft particle in a pure rotational flow

The first validation study considers the limit of a nearly rigid particle (i.e. Ca → 0 approaching zero), further referred to as quasi-rigid particle, suspended in a pure rotational flow. For the case of pure rotational flow, the fluid rate of deformation tensor $\boldsymbol{d}_f$ vanishes so that the fluid velocity gradient coincides with the fluid spin (vorticity) $\boldsymbol{l}_f \equiv \boldsymbol{w}_f$. In the case of pure rotational flow around the negative x_3-axis, the only non-zero elements of the fluid velocity gradient are $l_{f\,12} = -l_{f\,21} = \dot{\gamma}/2$. For validation, we compare our pseudo-rigid particle capture in the limiting case of quasi-rigid particles with our previously developed rigid particle solver, see [18]. To capture the quasi-rigid particle behavior, we set the capillary number to Ca = 0.0001 and the Reynolds number to Re = 0.1. Fig. 4 (a) shows excellent agreement in the dimensionless angular velocity $|\hat{\omega}_{s\,3}| = |\omega_{s\,3}|/\dot{\gamma}$ of the rigid and the quasi-rigid body while suspended in a pure rotational flow. As observed, both models reach the final angular velocity of $\omega_{s\,3} = \dot{\gamma}/2$, i.e. half the vorticity rate. Moreover, Fig. 4 (b) presents the evolution of the dimensionless torque $\hat{M} = M / \left[\mu^f \dot{\gamma} \, d_{eq}^3 \right]$, achieving again excellent agreement between the quasi-rigid particle (Ca → 0) and the rigid particle.

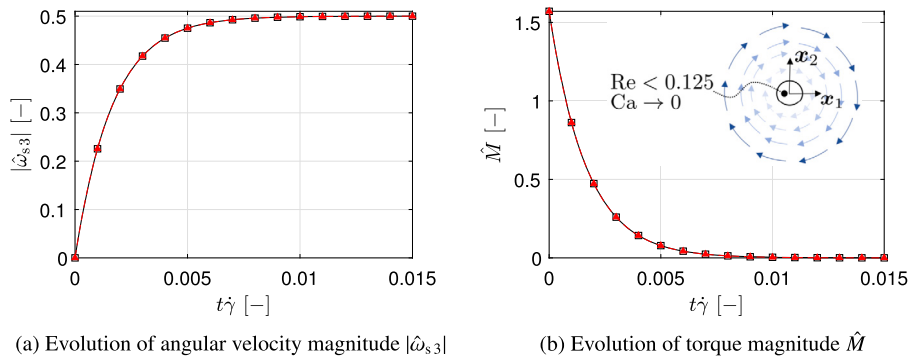(a) Evolution of angular velocity magnitude $|\hat{\omega}_{s\,3}|$

(b) Evolution of torque magnitude $\hat{M}$

Fig. 4. Comparison of $|\hat{\omega}_{s\,3}| = |\omega_{s\,3}|/\dot{\gamma}$ and $\hat{M} = M / \left[\mu^f \dot{\gamma} \, d_{eq}^3 \right]$ for a rigid and a quasi-rigid particle suspended in pure rotational flow. □ rigid particle, ▲ quasi-rigid deformable particle.

5.2. Soft particle in an extensional flow

In the second validation study we consider an elastic, initially spherical particle in an extension flow device, as used by Villone et al., [1]. The extensional flow device consists of two coaxial cylindrical tubes with dimensions: $D_1 = 700\,\mu m$, $D_2 = 234\,\mu m$, $L_1 = 1500\,\mu m$, $L_2 = 60\,\mu m$, $L_3 = 117\,\mu m$, see the sketch in Fig. 5 (a), [1]. The authors released the elastic bead at $x_3(0) = 1000\,mm$ and studied the translation and deformation of the soft particle. We employ the evolution of the fluid velocity gradient $l_{f\,33} = \partial u_3/\partial x_3$ as well as the particle velocity u_3 as provided by Villone et al., [1] to model the particle motion and deformation through the extensional flow device. Fig. 5 (a) displays the extracted data for the fluid velocity gradient $l_{f\,33}$ from Villone et al., [1], to which the elastic bead is subjected as it travels through the device. Furthermore, Fig. 5 (b) displays the obtained deformation parameter Đ as a function of the relative axial position $x_3 - x_3(0)$ of the reference results of Villone et al., [1], and the present model. As shown, by using the given

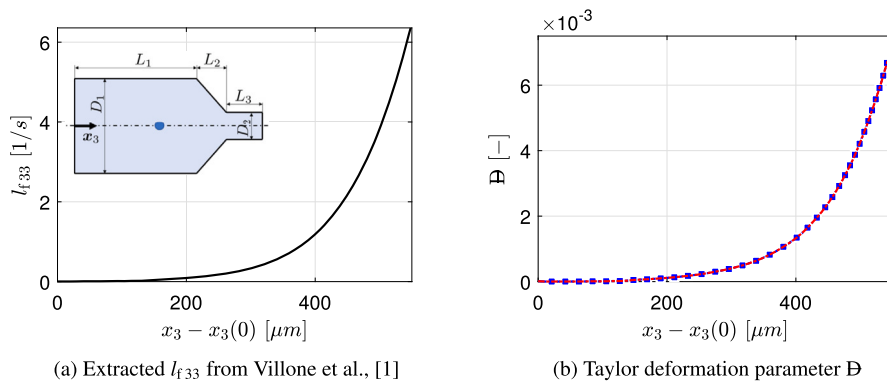(a) Extracted $l_{f\,33}$ from Villone et al., [1]

(b) Taylor deformation parameter Đ

Fig. 5. Elastic, initially spherical particle in an extensional flow. Fluid velocity gradient $l_{f\,33} = \partial u_3/\partial x_3$ (━) as provided by Villone et al., [1], and resulting deformation parameter Đ: ▬ Villone et al., [1], ▪▪ present model.

shear rate $l_{f\,33}$ (as function of $x_3 - x_3(0)$) and the provided particle velocity u_3, see [1], we achieve excellent agreement with the reference work and thus validate our model in the limit of extensional flow and small deformation. Fig. 5 also shows that the elastic deformation of the bead caused by the extensional flow due to the channel reduction becomes notable after $x_3 - x_3(0) > 200\,\mu m$, [1].

5.3. Soft particle in a simple shear flow

In this section, we study the three-dimensional problem of an elastic (neo-Hookean) particle of an initial spherical stress-free shape subjected to a simple shear flow ($l_{f\,12} = \dot{\gamma}$). In this context, we use the results of Gao et al., [37], as a reference. Gao et al. obtained a perfect agreement with the earlier results of Roscoe [34]. Note that for comparison with the viscoelastic results of Roscoe, Gao et al. neglected the viscous contribution present in Roscoe's solution. First, we compare the steady-state results of the particle deformation parameters ($Ð$, δ_1, δ_2, ϑ) as a function of capillary number Ca. In Fig. 6, the steady-state particle deformation parameters of an initially spherical neo-Hookean elastic particle in simple shear flow are shown. Fig. 6 (a) compares the steady state particle deformation parameter $Ð$ obtained by Gao et al. to the results obtained with the present model based on the equations of Jeffery-Roscoe. As shown, both Jeffery's model, [6], and Roscoe's model, [34], achieve excellent agreement with the results of Gao et al. for small deformations (Ca ≤ 0.2). Note that in this range the relationship between $Ð$ and Ca can be approximated as linear, [36]. However, for larger deformations (Ca > 0.2), the relationship between $Ð$ and Ca becomes nonlinear and the application of Jeffery's equations, [6], leads to large deviations. Nevertheless, using the corrections of Roscoe, [34], we achieve excellent agreement throughout the range of Ca numbers studied for $Ð$ as well as the aspect ratios δ_1, δ_2, see Fig. 6 (a, b).

(a) Steady-state deformation parameter $Ð$ (b) Steady state particle half axis ratios δ_1, δ_2

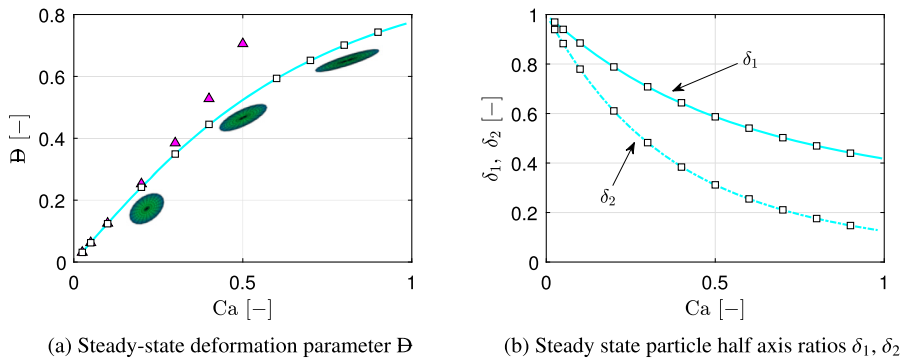**Fig. 6.** Steady state particle deformation parameter $Ð$ and aspect ratios $\delta_1 = b/a$ and $\delta_2 = c/a$ as a function of the capillary number Ca: ▬ Gao et al., [37], △ present model using Jeffery's equations, [6], □ present model using Roscoes's equations, [34].

In addition, Fig. 7 compares the steady-state particle orientation of the present model with the results of Gao et al., [37]. We reproduce their results accurately in the whole range of Ca numbers studied ($0 < $ Ca < 1). Note that the orientation of particles for arbitrary Ca numbers using Jeffery's equations, [6], yields $\vartheta = 45°$. This proves, that applying the original Jeffery's model without the Roscoe correction is not suitable for modeling particle orientation, even in the linear $Ð - $ Ca regime. This example is noteworthy as the soft particles display the phenomenon of tank-treading, i.e. stationary particle shape and orientation are achieved while inside the particle material keeps deforming as if being kneaded between two plates, [54]. Fig. 7 (b) displays the relation between particle softness and tank-treading frequency. Our modeling approach reveals that a higher particle deformability leads to a higher tank-treading frequency, where the lower limit (for Ca $\to 0$) coincides with half the flow vorticity ($\dot{\gamma}/2$), i.e. the angular velocity of a rigid particle.

(a) Steady state particle orientation ϑ (b) Normalized tank-treading frequency $|\hat{\omega}_{s,3}| = |\omega_{s\,3}|/\dot{\gamma}$
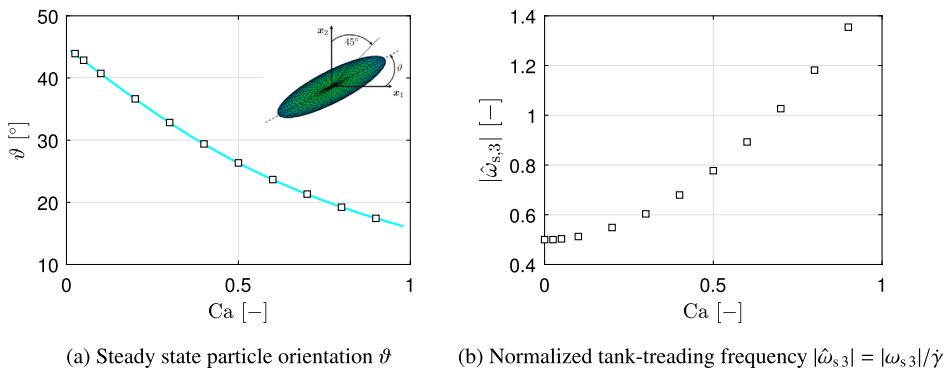
Fig. 7. Steady state particle orientation ϑ and tank-treading frequency $\omega_{s\,3}$ as a function of the capillary number Ca: ▬ Gao et al., [37], □ present model using Roscoes's equations, [34].

In a second step, we investigate the time-dependent solutions for initially spherical (three-dimensional) particles with a capillary number of Ca = 0.4, see Fig. 8. As shown in Fig. 8, our present deformable particle model can reproduce the evolution of the aspect ratios δ_1, δ_2 as well as the particle orientation ϑ of Gao et al. [37].
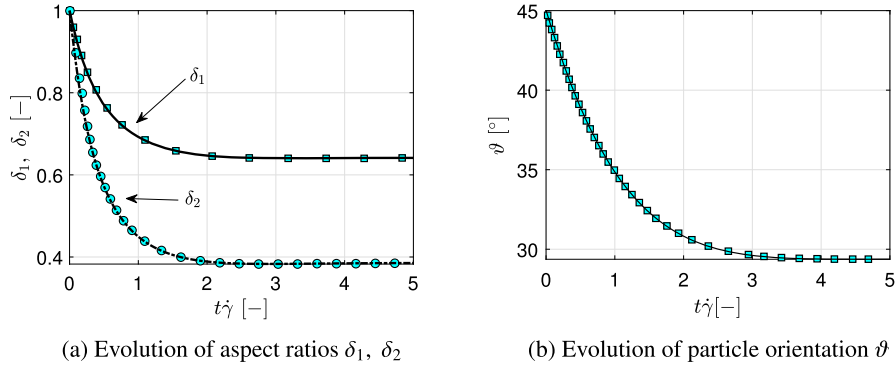

(a) Evolution of aspect ratios δ_1, δ_2 (b) Evolution of particle orientation ϑ

Fig. 8. Transient deformation and orientation of a neo-Hookean elastic particle (Ca = 0.4) suspended in simple shear flow: ▫/ ◯ Gao et al., [37], ▬ present model.

Furthermore, Fig. 9 visualizes the transient deformation, orientation as well as tank-treading motion of the deforming particle of Ca = 0.3, by highlighting the position of a material point during the deformation. As displayed, we observe that until $t\dot{\gamma} \leq 1.0$ the particle shape and orientation are changing significantly. From $t\dot{\gamma} \geq 1.0$ the change of particle orientation decreases strongly until steady-state shape and orientation are reached. Tank-treading motion can be observed from $t\dot{\gamma} > 1.0$, as the particle shape is quasi-stationary, however, the material point continues to change its position in the clockwise direction.
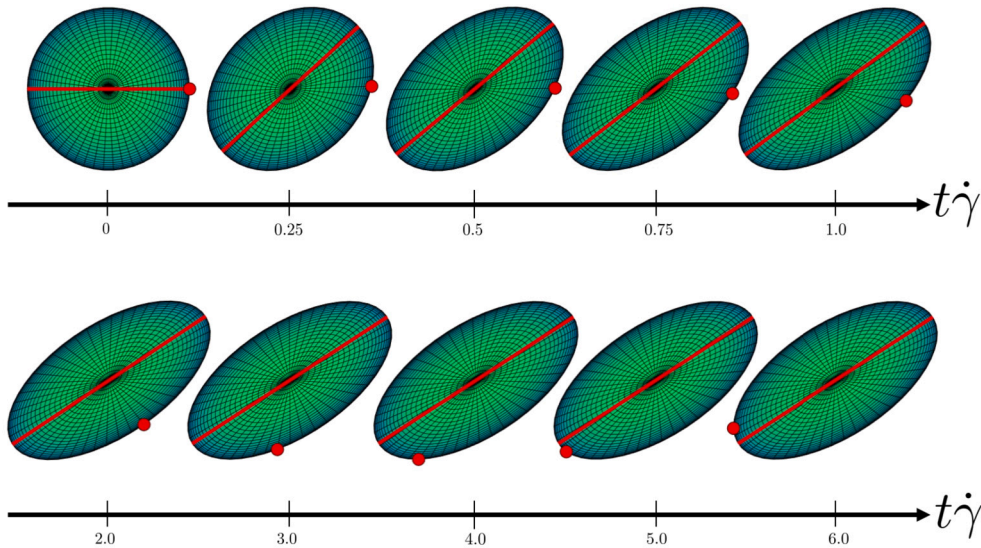
Fig. 9. Visualization of transient deformation and orientation of a neo-Hookean elastic particle (Ca = 0.3) suspended in simple shear flow. Tank-treading motion is observed and highlighting by tracking a chosen material point over time. Note that our approach is meshless and the displayed mesh is only for visualization purposes. See animation in supplementary material.

5.4. Soft particle in laminar pipe flow

Here we target the tracking of particles and their deformation in laminar pipe flow as employed by Tian et al., [64]. The case set-up is presented in Fig. 10. The Reynolds number of the flow is set to Re = 1. In agreement with Tian et al., [64], the fluid density is chosen as $\rho^f = 1.208\,kg/m^3$ and the kinematic viscosity as $\nu^f = 1.491 \times 10^{-5}\,m^2/s$. The diameter of the pipe is set to D = 4.2 mm. The particle volume equivalent diameter is chosen as $d_{eq} = 5\,\mu m$, and the particle density is set to $\rho_0^s = 2560\,kg/m^3$ for the sake of comparison to Tian et al., [64]. Note that the capillary number Ca in the following is defined based on $\dot{\gamma}_{max} = 923.8\,s^{-1}$ found at the pipe walls while the shear rate at the injection position is equal to $\dot{\gamma} = 725.9\,s^{-1}$.

Fig. 10. Sketch of the laminar pipe flow (Re = 1) set-up, with pipe diameter $D = 4.2\,mm$ and pipe length $L = 0.75\,m$. The gravitational direction points in the negative x_2 direction, while the streamwise direction is in positive x_1 direction. The initially spherical soft particle is released at $x_i = 0$, $i = 1, 2, 3$. The volume equivalent diameter of the particle is $d_{eq} = 5\,\mu m$ and the particle density is $\rho_0^s = 2560\,kg/m^3$.
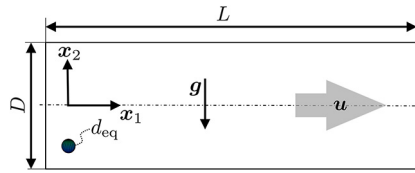
5.4.1. Quasi-rigid particle

In the first case, we compare a rigid particle to a quasi-rigid particle (Ca $\rightarrow$ 0) of initially spherical shape. The particles are injected at $(0,\ x_2(0),\ 0)$ with $x_2(0) = -1.65\,mm$ and tracked for $t = 0.1\,s$.

Fig. 11 displays the evolution of the direction cosines of a particle half axis with the streamwise direction x_1 and the spanwise direction x_2 for both the rigid as well as the quasi-rigid particle. As presented, the direction cosines of the quasi-rigid particle with negligible deformability (Ca = 0.0001) are in excellent agreement with the results obtained using the rigid particle.
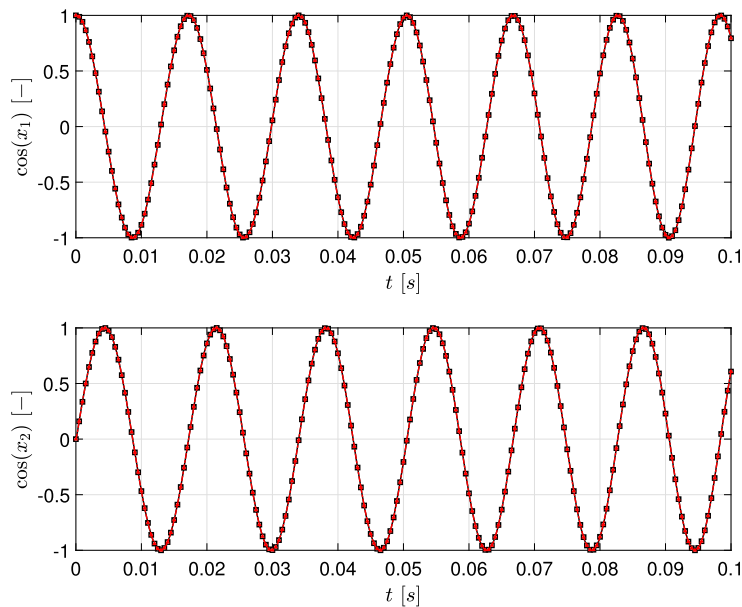

Fig. 11. Comparison of the direction cosines of rigid spherical particles and quasi-rigid spherical particle with negligible deformability (Ca = 0.0001) suspended in laminar pipe flow: □ rigid particle using the reference method [18], ▬ quasi-rigid particle (present model).

Furthermore, Fig. 12 (a-d) compares the resulting angular velocity around the x_3-axis ω_{s3} as well as the torque for both rigid and quasi-rigid particles. As observed, we obtain excellent agreement between the quasi-rigid and the rigid particle in their orientation dynamics. Furthermore, we observe that the particle angular velocity accelerates to around $\omega_{s3} = 363\,s^{-1}$, which is identical to the prescribed velocity gradient component l_{f12} at the injection position $(0,\ x_2(0),\ 0)$. These results prove the consistency of our pseudo-rigid body approach for particle tracking with a corresponding rigid body approach.

5.4.2. Soft deformable particle

In the second case, we study soft deformable particles that are injected at $(0,\ x_2(0),\ 0)$ with $x_2(0) = -1.65\,mm$. The particles are injected with zero velocity and angular velocity and are tracked until deposition. Fig. 13 (a-d) displays the trajectory and the velocities of the particles considered. Our approach demonstrates a strong dependency of the particle motion on its deformability. The particle with Ca = 0.25 possesses the largest settling velocity v_2, see Fig. 13 (d), and thus travels the least in the streamwise distance (Fig. 13 (b)). The softest particle considered, i.e. the particle with Ca = 1.0, possesses the lowest settling velocity (Fig. 13 (d)) and largest streamwise velocity (Fig. 13 (c)) and is thus able to achieve the largest traveling distance in x_1-direction, i.e. around 9866 d_{eq} further than the particle with Ca = 0.25. Note that the rigid particle reaches a final streamwise distance of 9165 d_{eq} and is in excellent agreement with the quasi-rigid particle (Ca = 0.0001) as the shape change for the quasi-rigid body is negligible. Furthermore, the rigid and quasi-rigid body settling velocity v_2 is in agreement with the terminal settling velocity of a sphere, see Fig. 13 (d).

Fig. 14 (a) presents a more detailed dependency of the maximal streamwise traveling distance and the particle deformability. We first observe a decrease in streamwise traveling distance towards low deformable particles (Ca <= 0.3). However, for particles with

(a) $|\hat{\omega}_{s\,3}|$

(b) $\hat{M}$ for $t \in [0,\,0.001]\,s$

(c) $|\hat{\omega}_{s\,3}|$ for $t \in [0.001,\,0.1]\,s$

(d) $\hat{M}$ for $t \in [0.001,\,0.1]\,s$
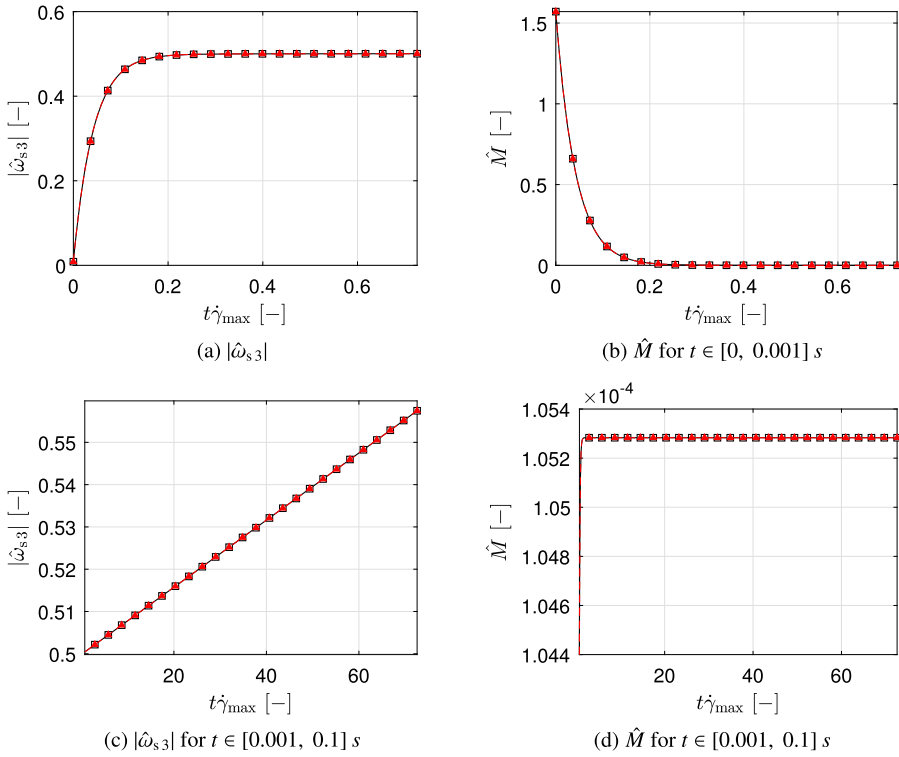
Fig. 12. Comparison of the angular velocity component $|\hat{\omega}_{s\,3}| = |\omega_{s\,3}|/\dot{\gamma}_{\max}$ with $\dot{\gamma}_{\max} = 923.8\,s^{-1}$ and torque $\hat{M} = M / \left[\mu^{f}\,\dot{\gamma}_{\max}\,d_{eq}^{3}\right]$ with $d_{eq} = 5\,\mu m$ of a rigid spherical particle and a quasi-rigid spherical particle with negligible deformability (Ca = 0.0001 suspended in laminar pipe flow: □ rigid particle using the reference method [18], ▬ quasi-rigid particle (present model).

(a)

(b)

(c)

(d)
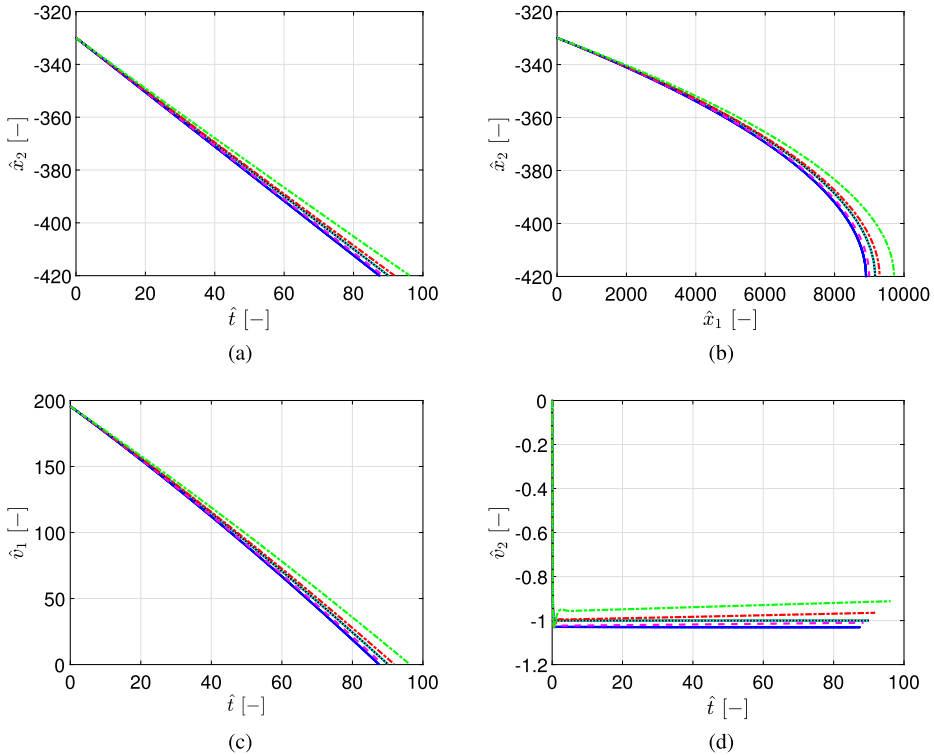
Fig. 13. Comparison of the trajectory ($\hat{x}_i = x_i/d_{eq}$ with $d_{eq} = 5\,\mu m$) and velocity ($\hat{v}_i = v_i/v_{sett}$ with the settling velocity $\boldsymbol{v}_{sett} = d_{eq}^2\left[\rho_0^s - \rho^f\right]\boldsymbol{g}/\left[18\nu^f\rho^f\right]$) of various soft deformable particles suspended in laminar pipe flow at position the initial position (0, $x_2(0)$, 0) with $x_2(0) = -1.65\,mm$. Note that $\hat{t} = d_{eq}/\boldsymbol{v}_{sett}$ and that the reference shear rate is chosen as $\dot{\gamma}_{\max} = 923.8\,s^{-1}$. ▪▪▪ rigid particle, ▬ Ca = 0.0001 (quasi-rigid particle), ▬ Ca = 0.25, ▬ Ca = 0.5, ▬ Ca = 0.75, ▬ Ca = 1.0.

(a) traveling distance in x_1

(b) tank-treading frequency ω_{s3} ($\omega_{s,ref}$)

Fig. 14. Dependence of the maximal traveling distance in $\hat{x}_{1\,max} = x_{1\,max}/d_{eq}$ as well as the tank-treading frequency ω_{s3} ($\omega_{s3\,ref}$: final rotation of rigid particle) on the particle softness: × rigid particle, □ Ca = 0.0001 − 1.0.

Ca > 0.35, the trend reverses and an increase in streamwise traveling distance is observed for softer particles. The maximum traveling distance displays an approximately linearly increasing dependency for particles with Ca >= 0.6 towards Ca >= 1.0. This phenomenon occurs due to the change of particle elongation as well as the particle orientation leading to altered drag forces in streamwise and gravitational directions.

In addition, Fig. 14 (b) shows the impact of particle softness on the tank-treading frequency. Our approach demonstrates that the higher the particle deformability the higher the tank-treading frequency with the lower limit (for Ca → 0) coinciding with the angular velocity of the rigid particle.

6. Conclusions

We presented a novel pseudo-rigid body approach for simulating the dynamics of initially spherical soft deformable micro-particles in dilute flows. For the sake of demonstration, we assume hyperelastic particles, however, our approach is entirely general in terms of the constitutive behavior of the particles. To induce the deformation of initially spherical particles to ellipsoids under the applied fluid flow-induced tractions, we employ the celebrated Jeffery-Roscoe model, [6,34].

The soft deformable particle tracking was validated through a series of pertinent benchmark test cases, including pure rotational flow, extensional flow, and simple shear flow conditions. I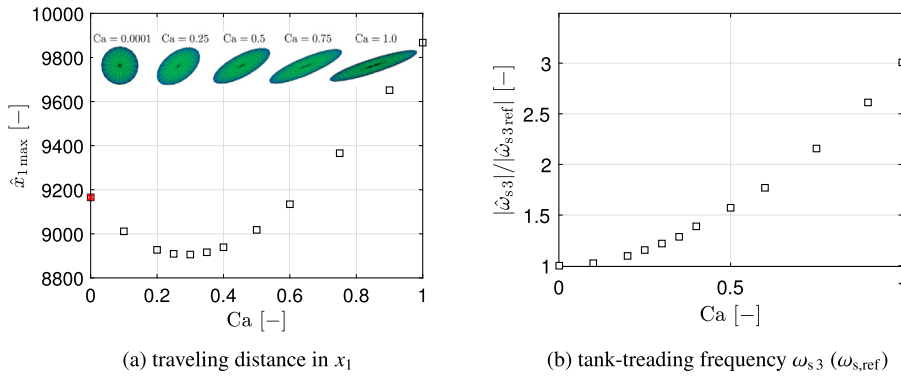n these investigations, we proved the excellent agreement between quasi-rigid particles, i.e. Ca → 0, and rigid particles in their orientational dynamics. Furthermore, for soft particles, we achieved excellent agreement in the barycentric and orientation dynamics in comparison with the reference results from the literature in extensional as well as simple shear flow conditions. As observed in the literature, we find that the micro-particles under investigation achieved a stationary ellipsoidal shape with a fixed orientation, while the material points within the soft micro-particle continuously move, i.e. the characteristic tank-treading phenomenon of soft deformable micro-particles suspended in flows. Furthermore, the obtained results highlight the importance of employing the Roscoe correction, [34], even for particles with low deformability (Ca < 0.2) in order to accurately predict the change in particle orientation.

In addition, the novel pseudo-rigid body approach enabled the study of the dependency of the particle trajectory on its deformability, while suspended in laminar pipe flow. In this context, we observed a strong dependency of the final particle position and the deposition time on the particle softness, highlighting the importance of accounting for the particle deformability.

Note that the results in the literature were obtained by using computationally costly discretizations as well as simplified assumptions such as limitation to incompressible and hyperelastic particles and specific flow conditions. On the contrary, our approach covers the whole range of macro-scale flow fields without limiting the material behavior of the particle and is thus utmost versatile. Our pseudo-rigid body algorithm is based on the point-particle assumption and therefore meshless and consequently computationally highly efficient (three degrees of freedom for the barycentric dynamics and only nine for the shape dynamics). Thus, the novel approach is suitable for tracking large numbers of soft deformable particles, while all surface discretization-based methods are strongly limited due to computational constraints.

Taken together, the developed novel pseudo-rigid body approach presents an utmost versatile and optimally efficient computational framework that can be applied within point-particle Lagrangian tracking of deformable micro-particles in dilute fluid flows.

CRediT authorship contribution statement

Jana Wedel: Writing – review & editing, Writing – original draft, Visualization, Validation, Software, Methodology, Investigation, Formal analysis, Data curation, Conceptualization. **Matjaž Hriberšek:** Writing – review & editing, Supervision, Resources, Methodology, Investigation, Formal analysis, Conceptualization. **Jure Ravnik:** Writing – review & editing, Supervision, Resources, Methodology, Investigation, Formal analysis, Conceptualization. **Paul Steinmann:** Writing – review & editing, Writing – original draft, Supervision, Resources, Project administration, Methodology, Investigation, Funding acquisition, Formal analysis, Conceptualization.

Declaration of competing interest

The authors declare that they have no known competing financial interests or personal relationships that could have appeared to influence the work reported in this paper.

Data availability

Data will be made available on request.

Acknowledgements

Appendix A. Rotational dynamics of a rigid body

Here, we sketch the transition from the equations of motion for the shape dynamics of a pseudo-rigid body to the equations of motion for the rotational dynamics of a rigid body. For a rigid body the deformation gradient $\boldsymbol{F}$ degenerates to the proper orthogonal tensor $\boldsymbol{R} \in \mathrm{SO}(3)$, i.e. the (continuum) rotation tensor. Note that $\boldsymbol{e}_a = \boldsymbol{R} \cdot \boldsymbol{E}_A$, $a \equiv A = 1, 2, 3$, thus $\boldsymbol{R} = \boldsymbol{e}_a \otimes \boldsymbol{E}_A = R_{aB}\, \boldsymbol{E}_B \otimes \boldsymbol{E}_A$ with $R_{aB} := \boldsymbol{e}_a \cdot \boldsymbol{E}_B$, $B = 1, 2, 3$, where $\boldsymbol{e}_a = R_{aB}\, \boldsymbol{E}_B$ and $\boldsymbol{E}_A = R_{bA}\, \boldsymbol{e}_b$ denote the (rotating) particle frame of reference and the (fixed) inertial frame of reference, respectively. Then $\boldsymbol{l}_s = \boldsymbol{A} \cdot \boldsymbol{R}^t$ and $\boldsymbol{A}$ with $\boldsymbol{A} = \dot{\boldsymbol{R}}$ compute as

$$\boldsymbol{l}_s =: \boldsymbol{w}_s = \boldsymbol{R} \cdot \boldsymbol{W} \cdot \boldsymbol{R}^t \quad \text{and} \quad \boldsymbol{A} =: \boldsymbol{w}_s \cdot \boldsymbol{R} = \boldsymbol{R} \cdot \boldsymbol{W}, \tag{A.1}$$

where $\boldsymbol{w}_s, \boldsymbol{W} \in \mathrm{SO}(3)$, respectively, are the skew-symmetric spatial and material spin tensors of the rigid body. Upon introducing the third-order spatial and material permutation tensors

$$\boldsymbol{e} = e_{abc}\, \boldsymbol{e}_a \otimes \boldsymbol{e}_b \otimes \boldsymbol{e}_c \quad \text{and} \quad \boldsymbol{E} = E_{ABC}\, \boldsymbol{E}_A \otimes \boldsymbol{E}_B \otimes \boldsymbol{E}_C, \tag{A.2}$$

where $e_{abc} = R_{aD}\, R_{bE}\, R_{cF}\, E_{DEF}$ and $E_{ABC} = R_{dA}\, R_{eB}\, R_{fC}\, e_{def}$ denote the fully skew-symmetric permutation symbol, the spin tensors $\boldsymbol{w}_s$ and $\boldsymbol{W}$ relate to their corresponding angular velocity vectors $\boldsymbol{\omega}_s$ and $\boldsymbol{\Omega}$, respectively, as

$$\boldsymbol{w}_s = -\boldsymbol{e} \cdot \boldsymbol{\omega}_s \quad \leftrightarrow \quad \boldsymbol{\omega}_s = -\frac{1}{2}\boldsymbol{e} : \boldsymbol{w}_s \quad \text{and} \quad \boldsymbol{W} = -\boldsymbol{E} \cdot \boldsymbol{\Omega} \quad \leftrightarrow \quad \boldsymbol{\Omega} = -\frac{1}{2}\boldsymbol{E} : \boldsymbol{W}, \tag{A.3}$$

where the properties $\boldsymbol{e} : \boldsymbol{e} = 2\,\boldsymbol{i}$ and $\boldsymbol{E} : \boldsymbol{E} = 2\,\boldsymbol{I}$, the spatial and material second-order unit tensors, and $\boldsymbol{e} \cdot \boldsymbol{e} = 2\,\mathbb{i}^{\mathrm{skw}}$ and $\boldsymbol{E} \cdot \boldsymbol{E} = 2\,\mathbb{I}^{\mathrm{skw}}$, the spatial and material skew-symmetric fourth-order unit tensors, hold. The spatial and material spin tensors and the corresponding angular velocity vectors are related as

$$\boldsymbol{w}_s = \boldsymbol{R} \cdot \boldsymbol{W} \cdot \boldsymbol{R}^t \quad \text{and} \quad \boldsymbol{\omega}_s = \boldsymbol{R} \cdot \boldsymbol{\Omega}, \tag{A.4}$$

transformation relations that due to the skew-symmetry of the spin tensors and the properties $\boldsymbol{w}_s \cdot \boldsymbol{\omega}_s = \boldsymbol{\omega}_s \times \boldsymbol{\omega}_s \equiv \boldsymbol{0}$ and $\boldsymbol{W} \cdot \boldsymbol{\Omega} = \boldsymbol{\Omega} \times \boldsymbol{\Omega} \equiv \boldsymbol{0}$ also hold for the time derivatives of the spatial and material spin tensors and the corresponding angular velocity vectors

$$\dot{\boldsymbol{w}}_s = \boldsymbol{R} \cdot \dot{\boldsymbol{W}} \cdot \boldsymbol{R}^t \quad \text{and} \quad \dot{\boldsymbol{\omega}}_s = \boldsymbol{R} \cdot \dot{\boldsymbol{\Omega}}. \tag{A.5}$$

Then, consistent with $\boldsymbol{w}_s^2 = \boldsymbol{R} \cdot \boldsymbol{W}^2 \cdot \boldsymbol{R}^t$, the time derivatives of $\boldsymbol{l}_s$ and $\boldsymbol{A} = \boldsymbol{l}_s \cdot \boldsymbol{R}$ expand as

$$\dot{\boldsymbol{l}}_s + \boldsymbol{l}_s^2 = \dot{\boldsymbol{w}}_s + \boldsymbol{w}_s^2 \quad \text{and} \quad \dot{\boldsymbol{A}} = \boldsymbol{R} \cdot [\dot{\boldsymbol{W}} + \boldsymbol{W}^2], \tag{A.6}$$

Taken together, with $\boldsymbol{P}(\boldsymbol{R}) \equiv \boldsymbol{0}$ and consequently $\boldsymbol{\sigma}(\boldsymbol{R}) \equiv \boldsymbol{0} \,\forall\, \boldsymbol{R} \in \mathrm{SO}(3)$ as well as with $\boldsymbol{\mathcal{M}} := \boldsymbol{R}^t \cdot \boldsymbol{M}$, a material tensor, the equation of motion for the shape dynamics of a pseudo-rigid body read in equivalent formats as

$$[\dot{\boldsymbol{w}}_s + \boldsymbol{w}_s^2] \cdot \boldsymbol{\theta} = \boldsymbol{m} \quad \text{and} \quad [\dot{\boldsymbol{W}} + \boldsymbol{W}^2] \cdot \boldsymbol{\Theta} = \boldsymbol{\mathcal{M}}. \tag{A.7}$$

Finally, projecting with the negative of the permutation tensors $\boldsymbol{e}$ and $\boldsymbol{E}$, respectively, results after tedious but straightforward algebraic manipulations in the familiar formats for the equation of motion governing the rotational dynamics of a rigid body

$$\boldsymbol{j} \cdot \dot{\boldsymbol{\omega}}_s + \boldsymbol{\omega}_s \times [\boldsymbol{j} \cdot \boldsymbol{\omega}_s] = \boldsymbol{t} \quad \text{and} \quad \boldsymbol{J} \cdot \dot{\boldsymbol{\Omega}} + \boldsymbol{\Omega} \times [\boldsymbol{J} \cdot \boldsymbol{\Omega}] = \boldsymbol{T}. \tag{A.8}$$

Here, with $\boldsymbol{B}_0 := \boldsymbol{R}^t \cdot \boldsymbol{b}_0$ and $\boldsymbol{T}_0 := \boldsymbol{R}^t \cdot \boldsymbol{t}_0$, material vectors, the external torque exerted on the rigid body follows as

$$\boldsymbol{t} := -\boldsymbol{e} : \boldsymbol{m} = \int_{B_t} \boldsymbol{\xi} \times \boldsymbol{b}_t \, \mathrm{d}v + \int_{\partial B_t} \boldsymbol{\xi} \times \boldsymbol{t}_t \, \mathrm{d}a \quad \text{and} \quad \boldsymbol{T} := -\boldsymbol{E} : \boldsymbol{\mathcal{M}} = \int_{B_0} \boldsymbol{\Xi} \times \boldsymbol{B}_0 \, \mathrm{d}V + \int_{\partial B_0} \boldsymbol{\Xi} \times \boldsymbol{T}_0 \, \mathrm{d}A \tag{A.9}$$

so that $\boldsymbol{t} = \boldsymbol{R} \cdot \boldsymbol{T}$ holds (since, e.g., $\boldsymbol{\Xi} \times \boldsymbol{B}_0 \, \mathrm{d}V = [\boldsymbol{R}^t \cdot \boldsymbol{\xi}] \times [\boldsymbol{R}^t \cdot \boldsymbol{b}_0] \, \mathrm{d}V = \boldsymbol{R}^t \cdot [\boldsymbol{\xi} \times \boldsymbol{b}_t] \, \mathrm{d}v$) and the spatial and material tensors of inertia $\boldsymbol{j}$ and $\boldsymbol{J}$ are related to the spatial and material Euler tensors $\boldsymbol{\theta}$ and $\boldsymbol{\Theta}$, respectively, as

$$j := [\theta : i]\,\theta - \theta = \int_{B_t} \rho^{\mathrm s} \left[|\xi|^2\, i - \xi \otimes \xi\right] \mathrm{d}v \quad \text{and} \quad J := [\Theta : I]\,\Theta - \Theta = \int_{B_0} \rho_0^{\mathrm s} \left[|\Xi|^2\, I - \Xi \otimes \Xi\right] \mathrm{d}V\,. \tag{A.10}$$

Observe that consistent with $\theta = R \cdot \Theta \cdot R^t$ and thus $\theta : i \equiv \Theta : I$ also $j = R \cdot J \cdot R^t$ holds. Summarizing, the transition from the equations of motion for the shape dynamics of a pseudo-rigid body to the equations of motion for the rotational dynamics of a rigid body can consistently be demonstrated for the rigidity limit $F \to R$.

Appendix B. Jeffery traction

The constant $\tilde p$ contributing to the Jeffery traction (fluctuation) $\tilde t_t$, [6], expands in terms of the constant fluid pressure p at a distance to the ellipsoid (reaction pressure to the incompressibility constraint for the fluid) and further parameters detailed below as

$$\tilde p = p + 4\,\mu^{\mathrm f}\left[\alpha_0\, A + \beta_0\, B + \gamma_0\, C\right]. \tag{B.1}$$

For ellipsoidal half axes $a \equiv r_1, b \equiv r_2, c \equiv r_3 > 0$ the parameters α_0, β_0, and γ_0 read as

$$\alpha_0 = \int_0^\infty \frac{1}{[a^2 + \Lambda]\,\Delta}\,\mathrm{d}\Lambda, \quad \beta_0 = \int_0^\infty \frac{1}{[b^2 + \Lambda]\,\Delta}\,\mathrm{d}\Lambda \quad \text{and} \quad \gamma_0 = \int_0^\infty \frac{1}{[c^2 + \Lambda]\,\Delta}\,\mathrm{d}\Lambda\,, \tag{B.2}$$

with $\Delta^2 := [a^2 + \Lambda][b^2 + \Lambda][c^2 + \Lambda]$. Furthermore, the parameters A, B, C read as

$$A = \frac{1}{6}\frac{2\,\alpha_0^\bullet\, d'_{11} - \beta_0^\bullet\, d'_{22} - \gamma_0^\bullet\, d'_{33}}{\alpha_0^\bullet\, \beta_0^\bullet + \beta_0^\bullet\, \gamma_0^\bullet + \gamma_0^\bullet\, \alpha_0^\bullet}\,,$$

$$B = \frac{1}{6}\frac{2\,\beta_0^\bullet\, d'_{22} - \gamma_0^\bullet\, d'_{33} - \alpha_0^\bullet\, d'_{11}}{\alpha_0^\bullet\, \beta_0^\bullet + \beta_0^\bullet\, \gamma_0^\bullet + \gamma_0^\bullet\, \alpha_0^\bullet}\,, \tag{B.3}$$

$$C = \frac{1}{6}\frac{2\,\gamma_0^\bullet\, d'_{33} - \alpha_0^\bullet\, d'_{11} - \beta_0^\bullet\, d'_{22}}{\alpha_0^\bullet\, \beta_0^\bullet + \beta_0^\bullet\, \gamma_0^\bullet + \gamma_0^\bullet\, \alpha_0^\bullet}\,.$$

Note that A, B, C depend on the coefficients $d'_{mn} = d'_{nm}$, $m,n = 1,2,3$ of the (modified) rate of deformation tensor $d := d_{\mathrm f} - d_{\mathrm s}$ (with $d_{\mathrm s} \equiv 0$ for a rigid ellipsoid) in the pFoR that is oriented along the ellipsoidal half axes as well as on the ellipsoidal half axes $a,b,c > 0$ as highlighted by the definition of the parameters $\alpha_0^\bullet$, $\beta_0^\bullet$, and $\gamma_0^\bullet$

$$\alpha_0^\bullet = \int_0^\infty \frac{\Lambda}{[b^2 + \Lambda][c^2 + \Lambda]\,\Delta}\,\mathrm{d}\Lambda, \quad \beta_0^\bullet = \int_0^\infty \frac{\Lambda}{[c^2 + \Lambda][a^2 + \Lambda]\,\Delta}\,\mathrm{d}\Lambda \quad \text{and} \quad \gamma_0^\bullet = \int_0^\infty \frac{\Lambda}{[a^2 + \Lambda][b^2 + \Lambda]\,\Delta}\,\mathrm{d}\Lambda\,. \tag{B.4}$$

The coefficients of $\tilde{\underline s}$ contributing to the Jeffery traction (fluctuation) $\tilde t_t$ expand in the pFoR that is oriented along the ellipsoidal half axes as

$$\tilde{\underline s}' = \frac{8}{a\,b\,c}\begin{bmatrix} A & H & G^\circ \\ H^\circ & B & F \\ G & F^\circ & C \end{bmatrix}. \tag{B.5}$$

Here, the parameters F, G, H and F°, G°, H° read as

$$F = \frac{\beta_0\, d'_{32} - c^2\, \alpha_0^\circ\, w'_{32}}{2\,\alpha_0^\circ\,[b^2\,\beta_0 + c^2\,\gamma_0]} \quad F^\circ = \frac{\gamma_0\, d'_{32} + b^2\, \alpha_0^\circ\, w'_{32}}{2\,\alpha_0^\circ\,[b^2\,\beta_0 + c^2\,\gamma_0]} \tag{B.6}$$

$$G = \frac{\gamma_0\, d'_{13} - a^2\, \beta_0^\circ\, w'_{13}}{2\,\beta_0^\circ\,[c^2\,\gamma_0 + a^2\,\alpha_0]} \quad G^\circ = \frac{\alpha_0\, d'_{13} + c^2\, \beta_0^\circ\, w'_{13}}{2\,\beta_0^\circ\,[c^2\,\gamma_0 + a^2\,\alpha_0]} \tag{B.7}$$

$$H = \frac{\alpha_0\, d'_{21} - b^2\, \gamma_0^\circ\, w'_{21}}{2\,\gamma_0^\circ\,[a^2\,\alpha_0 + b^2\,\beta_0]} \quad H^\circ = \frac{\beta_0\, d'_{21} + a^2\, \gamma_0^\circ\, w'_{21}}{2\,\gamma_0^\circ\,[a^2\,\alpha_0 + b^2\,\beta_0]}\,. \tag{B.8}$$

Note that F, G, H and F°, G°, H° depend on the coefficients $d'_{mn} = d'_{nm}$ and $w'_{mn} = -w'_{nm}$, $m,n = 1,2,3$ of the (modified) rate of deformation tensor $d := d_{\mathrm f} - d_{\mathrm s}$ (again with $d_{\mathrm s} \equiv 0$ for a rigid ellipsoid) and the modified spin (vorticity) tensor $w := w_{\mathrm f} - w_{\mathrm s}$ (with $w_{\mathrm s}$ related to the solid angular velocity vector $\omega_{\mathrm s} := \mathrm{axl}(w_{\mathrm s})$ for a rigid ellipsoid), respectively, all in the pFoR that is oriented along the ellipsoidal half axes, as well as on the ellipsoidal half axes $a,b,c > 0$ as highlighted by the definition of the parameters α_0°, β_0°, and γ_0°

$$\alpha_0^\circ = \int_0^\infty \frac{1}{[b^2 + \Lambda][c^2 + \Lambda]\,\Delta}\,\mathrm{d}\Lambda, \quad \beta_0^\circ = \int_0^\infty \frac{1}{[c^2 + \Lambda][a^2 + \Lambda]\,\Delta}\,\mathrm{d}\Lambda \quad \text{and} \quad \gamma_0^\circ = \int_0^\infty \frac{1}{[a^2 + \Lambda][b^2 + \Lambda]\,\Delta}\,\mathrm{d}\Lambda\,. \tag{B.9}$$

Finally, it is noted that the integrals for α_0, β_0, γ_0 are evaluated by a symbol manipulation code. Then α_0°, β_0°, γ_0° and $\alpha_0^\bullet$, $\beta_0^\bullet$, $\gamma_0^\bullet$ follow from [65]

$$\alpha_0^\circ = \frac{\gamma_0 - \beta_0}{b^2 - c^2}, \qquad \beta_0^\circ = \frac{\alpha_0 - \gamma_0}{c^2 - a^2} \qquad \text{and} \qquad \gamma_0^\circ = \frac{\beta_0 - \alpha_0}{a^2 - b^2},$$

$$\alpha_0^\bullet = \frac{b^2 \beta_0 - c^2 \gamma_0}{b^2 - c^2}, \quad \beta_0^\bullet = \frac{c^2 \gamma_0 - a^2 \alpha_0}{c^2 - a^2} \quad \text{and} \quad \gamma_0^\bullet = \frac{a^2 \alpha_0 - b^2 \beta_0}{a^2 - b^2}.$$

(B.10)

Remark *(Closed Form Expressions for Prolate Ellipsoids and Spheres)*. For prolate ellipsoids with $a > b \equiv c$ we obtain the closed form expressions:

$$\alpha_0 = -\frac{2}{a\,[a^2 - b^2]} + 2\frac{\cosh^{-1}(a/b)}{[a^2 - b^2]^{3/2}}, \qquad \beta_0 \equiv \gamma_0 = \frac{a}{b^2\,[a^2 - b^2]} - \frac{\cosh^{-1}(a/b)}{[a^2 - b^2]^{3/2}},$$

(B.11)

and consequently

$$\alpha_0^\circ = \frac{2\,a^3 - 5\,a\,b^2}{4\,b^4\,[a^2 - b^2]^2} + \frac{3\cosh^{-1}(a/b)}{4\,[a^2 - b^2]^{5/2}}, \qquad \beta_0^\circ \equiv \gamma_0^\circ = \frac{a^2 + 2b^2}{a\,b^2\,[a^2 - b^2]^2} - \frac{3\cosh^{-1}(a/b)}{[a^2 - b^2]^{5/2}},$$

(B.12)

as well as

$$\alpha_0^\bullet = \frac{-2\,a^5 + a^3\,b^2 - b^2\,\sqrt{a^2 - b^2}\,[b^2 - 4\,a^2]\cosh^{-1}(a/b) + a\,b^4}{4\,b^2\,[b^2 - a^2]^3},$$

$$\beta_0^\bullet \equiv \gamma_0^\bullet = \frac{-3\,a}{[a^2 - b^2]^2} + \frac{[2\,a^2 + b^2]\cosh^{-1}(a/b)}{[a^2 - b^2]^{5/2}}.$$

(B.13)

For spheres with $a \equiv b \equiv c$ these degenerate to the closed form expressions:

$$\alpha_0 \equiv \beta_0 \equiv \gamma_0 = \frac{2}{3\,a^3}, \quad \alpha_0^\circ \equiv \beta_0^\circ \equiv \gamma_0^\circ = \frac{2}{5\,a^5} \quad \text{and} \quad \alpha_0^\bullet \equiv \beta_0^\bullet \equiv \gamma_0^\bullet = \frac{4}{15\,a^3}.$$

(B.14)

Appendix C. Roscoe traction

With the aim to extend the traction (fluctuation) $\tilde{t}_t$ exerted by Stokes flow on an ellipsoidal rigid body, as derived by Jeffery [6], to an ellipsoidal and affinely deforming body, Roscoe [34], first rewrote Jeffery's expression for $\tilde{t}_t$ as

$$\tilde{t}_t = \underbrace{\left[-\tilde{p}(\boldsymbol{d}_\mathrm{f})\,\boldsymbol{i} + \mu^\mathrm{f}\,[\tilde{\boldsymbol{s}}(\boldsymbol{d}_\mathrm{f}, \boldsymbol{w}) - 2\,\boldsymbol{d}_\mathrm{f}]\right]\cdot\boldsymbol{n}}_{\text{perturbed near-field flow}} + \underbrace{2\,\mu^\mathrm{f}\,\boldsymbol{d}_\mathrm{f}\cdot\boldsymbol{n}}_{\text{undisturbed far-field flow}},$$

(C.1)

where $\boldsymbol{d}_\mathrm{f}$ denotes the rate of deformation tensor of the far-field flow, that, commensurate with the here assumed point-particle approach, is undisturbed by the presence of the ellipsoidal rigid body (recall also the definition of the modified spin (vorticity) tensor $\boldsymbol{w} := \boldsymbol{w}_\mathrm{f} - \boldsymbol{w}_\mathrm{s}$). The first two terms $\left[-\tilde{p}\,\boldsymbol{i} + \mu^\mathrm{f}\,[\tilde{\boldsymbol{s}} - 2\,\boldsymbol{d}_\mathrm{f}]\right]$ then capture the contribution by the perturbed near-field flow, i.e. perturbed due to the presence of an ellipsoidal rigid body, whereas the last term $2\,\mu^\mathrm{f}\,\boldsymbol{d}_\mathrm{f}$ is merely due to the undisturbed far-field flow. Then Roscoe [34] argued that the perturbed near-field flow due to an ellipsoidal deformable body is the same as that due to an ellipsoidal rigid body in a modified far-field flow, whereas the undisturbed far-field flow is unchanged. Concretely, he found that in order to capture the additional contribution to $\tilde{t}_t$ due to the deforming surface of an affinely deformable ellipsoidal body, $\boldsymbol{d}_\mathrm{f}$ in the Jeffery expression for the perturbed near-field flow need to be replaced by $\boldsymbol{d} := \boldsymbol{d}_\mathrm{f} - \boldsymbol{d}_\mathrm{s}$, whereas it remains unchanged in the undisturbed far-field flow. Taken together, this rationale renders eventually the remarkably simple final expression for the Roscoe traction (fluctuation) as

$$\tilde{t}_t = \left[-\tilde{p}(\boldsymbol{d})\,\boldsymbol{i} + \mu^\mathrm{f}\,[\tilde{\boldsymbol{s}}(\boldsymbol{d}, \boldsymbol{w}) + 2\,\boldsymbol{d}_\mathrm{s}]\right]\cdot\boldsymbol{n}.$$

(C.2)

Here, $\tilde{p}(\boldsymbol{d})$ and $\tilde{\boldsymbol{s}}(\boldsymbol{d})$ are as given by Jeffery [6], see Appendix B, when evaluated in terms of the modified far-field flow with rate of deformation tensor $\boldsymbol{d} := \boldsymbol{d}_\mathrm{f} - \boldsymbol{d}_\mathrm{s}$ (and spin (vorticity) tensor $\boldsymbol{w} := \boldsymbol{w}_\mathrm{f} - \boldsymbol{w}_\mathrm{s}$) in the pFoR that is oriented along the half axes of the deformed ellipsoid.

Appendix D. Brenner drag translational resistance tensor

For prolate spheroidal ellipsoids the coefficients of the translational resistance tensor $\boldsymbol{k}$ in the pFoR can be determined analytically and result in terms of their aspect ratio $\lambda := r_\mathrm{max}/r_\mathrm{min}$ with $r_\mathrm{max} = r_1 = a$ and $r_\mathrm{min} = r_2 = b \equiv r_3 = c$ as

$$k'_{11} = \frac{8\,[\lambda^2 - 1]^{3/2}}{[2\,\lambda^2 - 1]\ln\left(\lambda + \sqrt{\lambda^2 - 1}\right) - \lambda\sqrt{\lambda^2 - 1}},$$

(D.1)

$$k'_{22} \equiv k'_{33} = \frac{16 \left[\lambda^2 - 1\right]^{3/2}}{\left[2\,\lambda^2 - 3\right] \ln\left(\lambda + \sqrt{\lambda^2 - 1}\right) + \lambda\sqrt{\lambda^2 - 1}} \,. \tag{D.2}$$

For spheres $\boldsymbol{k}$ degenerates to a spherical tensor with $k'_{11} = k'_{22} = k'_{33} = 6$. For arbitrary superellipsoids (including general ellipsoids but also cube and diamond-like shapes) one can obtain the translational resistance coefficient matrix $\underline{k}'$ in the pFoR using the superellipsoid surrogate approach by Štrakl et al., [66,67]. The coefficient matrix $\underline{k}'$ of the translational resistance tensor $\underline{k}$ in the pFoR is related to its counterpart $\underline{k}$ in the iFoR via the rotation matrix $\underline{Q} := [Q_{aB}] = [\boldsymbol{n}_a \cdot \boldsymbol{E}_B]$ as

$$\underline{k}' = \underline{Q}\,\underline{k}\,\underline{Q}^T \,. \tag{D.3}$$

Appendix E. Algorithm: implicit-explicit time integrator

Initialize First Increment:
- Set $\boldsymbol{x}_c^0 = \boldsymbol{0}$, $\boldsymbol{v}_c^0 = \boldsymbol{0}$ and $\boldsymbol{F}^0 = \boldsymbol{1}$, $\boldsymbol{A}^0 = \boldsymbol{0}$ and $\boldsymbol{n}_a^0 = \boldsymbol{E}_A$, $Q_{aB}^0 = \delta_{aB}$, $r_a^0 = R$, $a, A, B = 1, 2, 3$

Increment Loop $\quad n = 0, \cdots, N - 1$

Pre-Process Increment:
- Read given fluid velocity and its spatial gradient from flow simulator $\boldsymbol{u}^{n+1}$ and $\boldsymbol{l}_{\mathrm{f}}^{n+1}$
- Compute coefficients in pFoR $l'^{\star}_{\mathrm{f}\,ab} = \boldsymbol{n}_a^n \cdot \boldsymbol{l}_{\mathrm{f}}^{n+1} \cdot \boldsymbol{n}_b^n$, $a, b = 1, 2, 3$
- Compute spatial solid velocity gradient $\boldsymbol{l}_{\mathrm{s}}^n = \boldsymbol{A}^n \cdot [\boldsymbol{F}^n]^{-1}$
- Compute coefficients in pFoR $l'^n_{\mathrm{s}\,ab} = \boldsymbol{n}_a^n \cdot \boldsymbol{l}_{\mathrm{s}}^n \cdot \boldsymbol{n}_b^n$, $a, b = 1, 2, 3$
- Compute Cauchy-type stress $\tilde{\sigma}^{\star} = \tilde{\sigma}(r_a^n, l'^n_{\mathrm{s}\,ab}, Q_{aB}^n; l'^{\star}_{\mathrm{f}\,ab})$ with $\tilde{\sigma}_{AB}^{\star} = \tilde{\sigma}'^{\star}_{mn} Q_{mA}^n Q_{nB}^n$, $a, A, B, m, n = 1, 2, 3$

Process Increment:
- Update distortion $\boldsymbol{F}^{n+1} = \arg\Big\{\boldsymbol{F}^{n+1} - \boldsymbol{F}^n - \Delta t\,\boldsymbol{A}^n - \Delta t^2\,\mathrm{vol}(\mathcal{B}_0)\left[\tilde{\boldsymbol{P}}^{\star}(\boldsymbol{F}^{n+1}; \tilde{\sigma}^{\star}) - \boldsymbol{P}(\boldsymbol{F}^{n+1})\right] \cdot \boldsymbol{\Theta}^{-1} \doteq \boldsymbol{0}\Big\}$
- Update mass-specific reduced gravity force $\boldsymbol{a}_{\mathrm{G}}^{n+1} = \beta_t(\boldsymbol{F}^{n+1})\,\boldsymbol{g}$
- Update Eulerian principal directions $\boldsymbol{n}_a^{n+1} = \mathrm{eigenvec}\Big\{\boldsymbol{F}^{n+1} \cdot [\boldsymbol{F}^{n+1}]^t\Big\}$, $a = 1, 2, 3$
- Update rotation matrix from iFoR to pFor $Q_{aB}^{n+1} = \boldsymbol{n}_a^{n+1} \cdot \boldsymbol{E}_B$, $a, B = 1, 2, 3$
- Update principal values $\lambda_a^{n+1} = \mathrm{eigenval}\Big\{\boldsymbol{F}^{n+1} \cdot [\boldsymbol{F}^{n+1}]^t\Big\}$, $a = 1, 2, 3$
- Update half axes $r_a^{n+1} = \lambda_a^{n+1} R$, $a = 1, 2, 3$
- Update drag resistance tensor $\boldsymbol{k}^{n+1} = \boldsymbol{k}(r_a^{n+1}, Q_{aB}^{n+1})$ with $k_{AB}^{n+1} = k'^{n+1}_{mn} Q_{mA}^{n+1} Q_{nB}^{n+1}$, $a, A, B, m, n = 1, 2, 3$
- Update barycenter position $\boldsymbol{x}_c^{n+1} = [\boldsymbol{i} + \Delta t/\tau_{\mathrm{D}}\,\boldsymbol{k}^{n+1}]^{-1} \cdot \left[\boldsymbol{x}_c^n + \Delta t\,\boldsymbol{v}_c^n + \Delta t^2\,\boldsymbol{a}_{\mathrm{G}}^{n+1} + \Delta t/\tau_{\mathrm{D}}\,\boldsymbol{k}^{n+1} \cdot [\Delta t\,\boldsymbol{u}^{n+1} + \boldsymbol{x}_c^n]\right]$

Post-Process Increment:
- Update $\boldsymbol{v}_c^{n+1} = [\boldsymbol{x}_c^{n+1} - \boldsymbol{x}_c^n]/\Delta t$
- Update $\boldsymbol{A}^{n+1} = [\boldsymbol{F}^{n+1} - \boldsymbol{F}^n]/\Delta t$

Initialize Next Increment:
- Set $\boldsymbol{x}_c^n \leftarrow \boldsymbol{x}_c^{n+1}$, $\boldsymbol{v}_c^n \leftarrow \boldsymbol{v}_c^{n+1}$ and $\boldsymbol{F}^n \leftarrow \boldsymbol{F}^{n+1}$, $\boldsymbol{A}^n \leftarrow \boldsymbol{A}^{n+1}$ and $\boldsymbol{n}_a^n \leftarrow \boldsymbol{n}_a^{n+1}$, $Q_{aB}^n \leftarrow Q_{aB}^{n+1}$, $r_a^n \leftarrow r_a^{n+1}$, $a, B = 1, 2, 3$

End Increment Loop

Note that the employed Newton Raphson converges quadratically and typically in 3 iterations to take the residual below 1e-12.

Appendix F. Discussion on the efficiency of the novel pseudo-rigid particle approach

In order to assess the efficiency of the novel pseudo-rigid approach to soft particles, we here compare the computational effort to more standard discretization approaches such as for example the boundary element method (boundary only discretization) or the finite element method (volume discretization).

We would like to point out that, based on our own experience with discretizing (rigid) particles (see [18]), we have found that a surface mesh for a boundary element discretization with about 3000 elements is required for a reasonable shape approximation. If we combine this with a volume discretization, the computational effort increases even more drastically. Table F.1 presents selected particles employed in [18] alongside the corresponding required mesh resolution and computational time. As highlighted, for a spherical particle, i.e. a particle with aspect ratios $\lambda_1 = \lambda_2 = 1$, we required 3206 elements, and the computation time to determine

Table F.1
Computation time for specific particles employed in our previous work, see [18].

Particles	λ_1	λ_2	n[1]	t [s]
1	1	1	3206	56
2	3	1	3254	70
3	4	2	3998	120

[1] Number of mesh elements.

the surface tractions in our boundary element code was 56 seconds. For a prolate ellipsoid with $\lambda_1 = 3$, $\lambda_2 = 1$, we required a mesh element count of 3254 and a simulation time of 70 s. For a triaxial ellipsoid with $\lambda_1 = 4$, $\lambda_2 = 2$, we require 3998 mesh elements and a simulation time of 120 s to obtain the forces exerted on the particle surface. Furthermore, if the particle shape changes and the particle elongates due to the surface tractions an adaptive algorithm would be required to adjust the particle mesh during the simulation, which would further increase the computational effort. To conclude, we estimated that a particle resolved simulation would require an additional computational time of the order of 10^2 seconds per particle per time step. This makes such an approach infeasible for large number of particles. In contrast, our point particle approach, requires approximately 0.00030 s per particle per time step making it possible to run simulations with millions of particles.

To summarize, compared to the computational burden when the particle is discretized, our novel pseudo-rigid body approach comes at negligible costs.

References

[1] M. Villone, J. Nunes, Y. Li, H. Stone, P.L. Maffettone, Design of a microfluidic device for the measurement of the elastic modulus of deformable particles, Soft Matter 15 (2019) 880–889, https://doi.org/10.1039/C8SM02272K.

[2] A. Einstein, Eine neue Bestimmung der Moleküldimensionen, Ann. Phys. 324 (2) (1906) 289–306.

[3] G.K. Batchelor, J.T. Green, The determination of the bulk stress in a suspension of spherical particles to order c2, J. Fluid Mech. 56 (3) (1972) 401–427, https://doi.org/10.1017/S0022112072002435.

[4] H. Brenner, Rheology of a dilute suspension of axisymmetric Brownian particles, Int. J. Multiph. Flow 1 (2) (1974) 195–341, https://doi.org/10.1016/0301-9322(74)90018-4, https://www.sciencedirect.com/science/article/pii/0301932274900184.

[5] A.B. Subramaniam, M. Abkarian, L. Mahadevan, H. Stone, Non-spherical bubbles, Nature 438 (2005) 209–237.

[6] G. Jeffery, The motion of ellipsoidal particles immersed in a viscous fluid, Proc. R. Soc. Lond. Ser. A, Contain. Pap. Math. Phys. Character 102 (715) (1922) 161–179, https://doi.org/10.1098/rspa.1922.0078.

[7] I.M. Krieger, Rheology of monodisperse latices, Adv. Colloid Interface Sci. 3 (2) (1972) 111–136, https://doi.org/10.1016/0001-8686(72)80001-0.

[8] I. Zarraga, D. Hill Jr., Erratum: "The characterization of the total stress of concentrated suspensions of noncolloidal spheres in Newtonian fluids" [J. Rheol. 44 (2000) 185–220], J. Rheol. 44 (2000) 185–220, https://doi.org/10.1122/1.551083.

[9] B. Snook, L.M. Davidson, J.E. Butler, O. Pouliquen, E. Guazzelli, Normal stress differences in suspensions of rigid fibres, J. Fluid Mech. 758 (2014) 486–507, https://doi.org/10.1017/jfm.2014.541.

[10] P.G. Koullapis, S.C. Kassinos, M.P. Bivolarova, A.K. Melikov, Particle deposition in a realistic geometry of the human conducting airways: effects of inlet velocity profile, inhalation flowrate and electrostatic charge, J. Biomech. 49 (11) (2016) 2201–2212, https://doi.org/10.1016/j.jbiomech.2015.11.029.

[11] F. Lizal, M. Cabalka, M. Maly, J. Elcner, M. Belka, E.L. Sujanska, A. Farkas, P. Starha, O. Pech, O. Misik, J. Jedelsky, M. Jicha, On the behavior of inhaled fibers in a replica of the first airway bifurcation under steady flow conditions, Aerosol Sci. Technol. 56 (4) (2022) 367–381, https://doi.org/10.1080/02786826.2022.2027334.

[12] G. Bossis, J.F. Brady, Dynamic simulation of sheared suspensions. I. General method, J. Chem. Phys. 80 (1984) 5141–5154.

[13] S. Gallier, E. Lemaire, L. Lobry, F. Peters, A fictitious domain approach for the simulation of dense suspensions, J. Comput. Phys. 256 (2014) 367–387, https://doi.org/10.1016/j.jcp.2013.09.015.

[14] J. Butler, B. Snook, Microstructural dynamics and rheology of suspensions of rigid fibers, Annu. Rev. Fluid Mech. 50 (2018) 299–318, https://doi.org/10.1146/annurev-fluid-122316-045144.

[15] J. Wedel, M. Štrakl, P. Steinmann, M. Hriberšek, J. Ravnik, Can CFD establish a connection to a milder COVID-19 disease in younger people?, Comput. Mech. 67 (2021) 1497–1513, https://doi.org/10.1007/s00466-021-01988-5.

[16] J. Wedel, P. Steinmann, M. Štrakl, M. Hriberšek, J. Ravnik, Risk assessment of infection by airborne droplets and aerosols at different levels of cardiovascular activity, Arch. Comput. Methods Eng. 28 (6) (2021) 4297–4316, https://doi.org/10.1007/s11831-021-09613-7.

[17] J. Wedel, P. Steinmann, M. Štrakl, M. Hriberšek, Y. Cui, J. Ravnik, Anatomy matters: the role of the subject-specific respiratory tract on aerosol deposition - a CFD study, Comput. Methods Appl. Mech. Eng. 401 (2022) 115372.

[18] J. Wedel, P. Steinmann, M. Štrakl, M. Hriberšek, J. Ravnik, Shape matters: Lagrangian tracking of complex nonspherical microparticles in superellipsoidal approximation, Int. J. Multiph. Flow 158 (2023) 104283, https://doi.org/10.1016/j.ijmultiphaseflow.2022.104283.

[19] J. Ravnik, M. Štrakl, J. Wedel, P. Steinmann, M. Hriberšek, Stokes flow induced drag and torque on asbestos-like fibres can not be estimated by a simplistic ellipsoidal approximation, in: 45th International Conference on Boundary Elements and Other Mesh Reduction Methods Organized by WIT - Wessex Institute of Technology, U.K., 2022.

[20] S.P. Thampi, K. Stratford, O. Henrich, Simulating dynamics of ellipsoidal particles using lattice Boltzmann method, Phys. Rev. E 109 (2024) 065302, https://doi.org/10.1103/PhysRevE.109.065302, https://link.aps.org/doi/10.1103/PhysRevE.109.065302.

[21] D. Silva, R. Coelho, I. Pagonabarraga, S. Succi, M. Telo da Gama, N. Araujo, Lattice Boltzmann simulation of deformable fluid-filled bodies: progress and perspectives, Soft Matter 20 (2024) 2419.

[22] C. Pozrikidis (Ed.), Modeling and Simulation of Capsules and Biological Cells, CRC Mathematical Biology & Medicine Series, vol. 2, Chapman & Hall, 2003.

[23] I. Galaev, B. Mattiasson, Smart Polymers: Applications in Biotechnology and Biomedicine, vol. 20, CRC Press, 2007.

[24] C. Porcaro, M. Saeedipour, Unresolved RBCs: an upscaling strategy for the CFD-DEM simulation of blood flow with deformable cells, Comput. Biol. Med. 181 (2024) 109081, https://doi.org/10.1016/j.compbiomed.2024.109081.

[25] P.K. Sanagavarapu, G. Subramanian, P.R. Nott, Shape dynamics and rheology of dilute suspensions of elastic and viscoelastic particles, J. Fluid Mech. 949 (2022) A22, https://doi.org/10.1017/jfm.2022.704.

[26] G. Lu, J. Third, C. Müller, Critical assessment of two approaches for evaluating contacts between super-quadric shaped particles in dem simulations, Chem. Eng. Sci. 78 (2012) 226–235, https://doi.org/10.1016/j.ces.2012.05.041.

[27] A. Podlozhnyuk, S. Pirker, C. Kloss, Efficient implementation of superquadric particles in discrete element method within an open-source framework, Comput. Part. Mech. 4 (2017), https://doi.org/10.1007/s40571-016-0131-6.

[28] H. Frohlich, R. Sack, Theory of the rheological properties of dispersions, Proc. R. Soc. Lond. 185 (1946) 415–430.

[29] R. Cerf, On the frequency dependence of the viscosity of high polymer solutions, J. Chem. Phys. 20 (3) (1952) 395–402.

[30] J.G. Oldroyd, The elastic and viscous properties of emulsions and suspensions, Proc. R. Soc. Lond. Ser. A, Math. Phys. Sci. 218 (1953) 122–132.

[31] J.D. Eshelby, The determination of the elastic field of an ellipsoidal inclusion, and related problems, Proc. R. Soc. Lond. 241 (1957) 376–396.

[32] J.D. Eshelby, The elastic eld outside an ellipsoidal inclusion, Proc. R. Soc. Lond. 252 (1959) 561–569.

[33] J. Goddard, C. Miller, Nonlinear effects in the rheology of dilute suspensions, J. Fluid Mech. 28 (1967) 657–673.

[34] R. Roscoe, On the rheology of a suspension of viscoelastic spheres in a viscous liquid, J. Fluid Mech. 28 (2) (1967) 273–293, https://doi.org/10.1017/S002211206700206X.

[35] T. Murata, Deformation of an elastic particle suspended in an arbitrary flow field, J. Phys. Soc. Jpn. 50 (3) (1981) 1009–1016.

[36] T. Gao, H.H. Hu, Deformation of elastic particles in viscous shear flow, J. Comput. Phys. 228 (6) (2009) 2132–2151, https://doi.org/10.1016/j.jcp.2008.11.029.

[37] T. Gao, H.H. Hu, P.P. Castañeda, Rheology of a suspension of elastic particles in a viscous shear flow, J. Fluid Mech. 687 (2011) 209–237, https://doi.org/10.1017/jfm.2011.347.

[38] T. Gao, H. Hu, P. Castañeda, Shape dynamics and rheology of soft elastic particles in a shear flow, Phys. Rev. Lett. 108 (2012) 058302, https://doi.org/10.1103/PhysRevLett.108.058302.

[39] T. Gao, H. Hu, P. Castañeda, Dynamics and rheology of elastic particles in an extensional flow, J. Fluid Mech. 715 (2013) 573–596.

[40] D. De Marinis, A. Mantegazza, A. Coclite, M.D. de Tullio, A fluid-structure interaction method for soft particle transport in curved microchannels, Comput. Methods Appl. Mech. Eng. 418 (2024) 116592, https://doi.org/10.1016/j.cma.2023.116592, https://www.sciencedirect.com/science/article/pii/S0045782523007168.

[41] M.E. Rosti, L. Brandt, Suspensions of deformable particles in a Couette flow, in: XVIIIth International Workshop on Numerical Methods for Non-Newtonian Flows, June 12-15 2017, Vancouver, Canada, J. Non-Newton. Fluid Mech. 262 (2018) 3–11, https://doi.org/10.1016/j.jnnfm.2018.01.008, https://www.sciencedirect.com/science/article/pii/S0377025717304718.

[42] T. Jeewandara, Using flexible microparticles as drug carriers to shuttle nanoparticles to the vascular wall, Tech. Rep., 2021, https://phys.org/news/2021-05-flexible-microparticles-drug-carriers-shuttle.html.

[43] L. Sercombe, T. Veerati, F. Moheimani, S.Y.-Y. Wu, A.K. Sood, S. Hua, Advances and challenges of liposome assisted drug delivery, Front. Pharmacol. 6 (2015) 286.

[44] D. Guimaraes, A. Cavaco-Paulo, E. Nogueira, Design of liposomes as drug delivery system for therapeutic applications, Int. J. Pharm. 601 (2021) 120571.

[45] D. Barthès-Biesel, Motion of a spherical microcapsule freely suspended in a linear shear flow, J. Fluid Mech. 100 (4) (1980) 831–853.

[46] D. Barthès-Biesel, J.M. Rallison, The time-dependent deformation of a capsule freely suspended in a linear shear flow, J. Fluid Mech. 113 (1981) 251–267, https://doi.org/10.1017/S0022112081003480.

[47] M. Kraus, W. Wintz, U. Seifert, R. Lipowsky, Fluid vesicles in shear flow, Phys. Rev. Lett. 77 (17) (1996) 3685–3688.

[48] M. Abkarian, A. Viallat, Dynamics of vesicles in a wall-bounded shear flow, Biophys. J. 89 (2) (2005) 1055–1066, https://doi.org/10.1529/biophysj.104.056036.

[49] H. Zhao, E. Shaqfeh, V. Narsimhan, Shear-induced particle migration and margination in a cellular suspension, Phys. Fluids 24 (2012), https://doi.org/10.1063/1.3677935.

[50] M. Guedda, M. Benlahsen, C. Misbah, Rheological properties of a vesicle suspension, Phys. Rev. E 90 (2014) 052302, https://doi.org/10.1103/PhysRevE.90.052302.

[51] A. Laadhari, A. Deeb, Computational modeling of individual red blood cell dynamics using discrete flow composition and adaptive time-stepping strategies, Symmetry 15 (2023) 1138, https://doi.org/10.3390/sym15061138.

[52] H. Zhao, J.B. Freund, R.D. Moser, A fixed-mesh method for incompressible flow–structure systems with finite solid deformations, J. Comput. Phys. 227 (6) (2008) 3114–3140, https://doi.org/10.1016/j.jcp.2007.11.019, https://www.sciencedirect.com/science/article/pii/S0021999107005116.

[53] B. Nasouri, A. Khot, G.J. Elfring, Elastic two-sphere swimmer in Stokes flow, Phys. Rev. Fluids 2 (4) (2017) 101.

[54] R. Gerum, E. Mirzahossein, M. Eroles, J. Elsterer, A. Mainka, A. Bauer, S. Sonntag, A. Winterl, J. Bartl, L. Fischer, S. Abuhattum, R. Goswami, S. Girardo, J. Guck, S. Schrüfer, N. Ströhlein, M. Nosratlo, H. Herrmann, D. Schultheis, F. Rico, S.J. Müller, S. Gekle, B. Fabry, Viscoelastic properties of suspended cells measured with shear flow deformation cytometry, eLife 11 (2022) e78823, https://doi.org/10.7554/eLife.78823.

[55] M.M. Villone, M. Trofa, M.A. Hulsen, P.L. Maffettone, Numerical design of a t-shaped microfluidic device for deformability-based separation of elastic capsules and soft beads, Phys. Rev. E 96 (2017) 053103, https://doi.org/10.1103/PhysRevE.96.053103, https://link.aps.org/doi/10.1103/PhysRevE.96.053103.

[56] H. Cohen, R.G. Muncaster, The Theory of Pseudo-Rigid Bodies, vol. 33, Springer Tracts in Natural Philosophy, 1988.

[57] C.T. Crowe, J.D. Schwarzkopf, M. Sommerfeld, Y. Tsuji, Multiphase Flows with Droplets and Particles, CRC Press, 2011.

[58] J.G.M. Kuerten, Point-particle DNS and LES of particle-laden turbulent flow - a state-of-the-art review, Flow Turbul. Combust. 97 (3) (2016) 689–713.

[59] H. Brenner, The Stokes resistance of an arbitrary particle, Chem. Eng. Sci. 18 (1963) 1–25.

[60] P. Steinmann, Spatial and Material Forces in Nonlinear Continuum Mechanics, vol. 272, Springer, 2022.

[61] H. Brenner, The Stokes resistance of an arbitrary particle-IV arbitrary fields of flow, Chem. Eng. Sci. 19 (10) (1964) 703–727, https://doi.org/10.1016/0009-2509(64)85084-3.

[62] H. Brenner, The Stokes resistance of an arbitrary particle-III. Shear fields, Chem. Eng. Sci. 19 (9) (1964) 631–651, https://doi.org/10.1016/0009-2509(64)85052-1.

[63] H. Stone, Dynamics of drop deformation and breakup in viscous flows, Annu. Rev. Fluid Mech. 26 (1994) 65–102.

[64] L. Tian, G. Ahmadi, Z. Wang, P.K. Hopke, Transport and deposition of ellipsoidal fibers in low Reynolds number flows, J. Aerosol Sci. 45 (2012) 1–18, https://doi.org/10.1016/j.jaerosci.2011.09.001.

[65] J. Jezek, S. Saic, K. Segeth, Numerical modeling of the movement of a rigid particle in viscous fluid, Appl. Math. 44 (1999) 469–479.

[66] M. Štrakl, M. Hriberšek, J. Wedel, P. Steinmann, J. Ravnik, A model for translation and rotation resistance tensors for superellipsoidal particles in Stokes flow, J. Mar. Sci. Eng. 10 (3) (2022) 369.

[67] M. Štrakl, J. Wedel, P. Steinmann, M. Hriberšek, J. Ravnik, Tensor coefficient model for superellipsoids, https://github.com/transport-phenomena/superellipsoid-force-torque-model. (Accessed 3 February 2022).